



HAL
open science

Mountain wave PSC dynamics and microphysics from ground-based lidar measurements and meteorological modeling

J. Reichardt, A. Dörnbrack, S. Reichardt, P. Yang, T. J. Mcgee

► **To cite this version:**

J. Reichardt, A. Dörnbrack, S. Reichardt, P. Yang, T. J. Mcgee. Mountain wave PSC dynamics and microphysics from ground-based lidar measurements and meteorological modeling. *Atmospheric Chemistry and Physics Discussions*, 2003, 3 (6), pp.5831-5873. hal-00301377

HAL Id: hal-00301377

<https://hal.science/hal-00301377>

Submitted on 18 Jun 2008

HAL is a multi-disciplinary open access archive for the deposit and dissemination of scientific research documents, whether they are published or not. The documents may come from teaching and research institutions in France or abroad, or from public or private research centers.

L'archive ouverte pluridisciplinaire **HAL**, est destinée au dépôt et à la diffusion de documents scientifiques de niveau recherche, publiés ou non, émanant des établissements d'enseignement et de recherche français ou étrangers, des laboratoires publics ou privés.

Mountain wave PSC dynamics and microphysics from ground-based lidar measurements and meteorological modeling

J. Reichardt^{1, 2, *}, A. Dörnbrack³, S. Reichardt^{1, 2}, P. Yang⁴, and T. J. McGe²

¹Joint Center for Earth Systems Technology, University of Maryland Baltimore County, Baltimore, Maryland, USA

²Atmospheric Chemistry and Dynamics Branch, NASA Goddard Space Flight Center, Greenbelt, Maryland, USA

³Institut für Physik der Atmosphäre, Deutsches Zentrum für Luft- und Raumfahrt (DLR) Oberpfaffenhofen, Weßling, Germany

⁴Department of Atmospheric Sciences, Texas A&M University, College Station, Texas, USA

*now at Meteorologisches Observatorium Lindenberg, Deutscher Wetterdienst, Tauche, Germany

Received: 20 August 2003 – Accepted: 12 November 2003 – Published: 18 November 2003

Correspondence to: J. Reichardt (jens.reichardt@dwd.de)

**Mountain wave PSC
dynamics and
microphysics**

J. Reichardt et al.

Title Page

Abstract

Introduction

Conclusions

References

Tables

Figures

◀

▶

◀

▶

Back

Close

Full Screen / Esc

Print Version

Interactive Discussion

© EGU 2003

Abstract

The exceptional day-long observation of a polar stratospheric cloud (PSC) by two ground-based lidars at the Swedish research facility Esrange (67.9° N, 21.1° E) on 16 January 1997 is analyzed in terms of PSC dynamics and microphysics. Mesoscale meteorological modeling is utilized to resolve the time-space ambiguity of the lidar measurements. Microphysical properties of the PSC particles are retrieved by comparing the measured particle depolarization ratio and the PSC-averaged lidar ratio with theoretical optical data derived for different particle shapes. In the morning, nitric acid trihydrate (NAT) particles and then increasingly coexisting liquid ternary aerosol (LTA) were detected as outflow from a mountain wave-induced ice PSC upwind Esrange. The NAT PSC consisted of irregular-shaped particles with length-to-diameter ratios between 0.75 and 1.25, maximum dimensions from 0.7 to 0.9 μm , and a number density from 8 to 12 cm^{-3} and the coexisting LTA droplets had diameters from 0.7 to 0.9 μm , a refractive index of 1.39 and a number density from 7 to 11 cm^{-3} . NAT activation was probably substantial ($\sim 53\%$) which appears to be the effect of the high cooling rates ($> 100 \text{ K/h}$) in the stratospheric mountain wave. The total amount of condensed HNO_3 was in the range of 57–90% of the HNO_3 gas reservoir. By early afternoon the mountain wave-induced ice PSC expanded above the lidar site. Its optical data indicate a decrease in minimum particle size from 4.3 to 1.9 μm with time, possibly due to a diminishing growth rate. Later on, following the cessation of particle nucleation upwind wave-processed LTA was observed only. Our study demonstrates that ground-based lidar measurements of PSCs can be comprehensively interpreted if combined with mesoscale meteorological data.

1. Introduction

Lidar measurements have proven valuable in polar stratospheric cloud (PSC) research, yet their interpretation is often complicated. Retrieval of PSC microphysical properties

Mountain wave PSC dynamics and microphysics

J. Reichardt et al.

Title Page

Abstract

Introduction

Conclusions

References

Tables

Figures

◀

▶

◀

▶

Back

Close

Full Screen / Esc

Print Version

Interactive Discussion

**Mountain wave PSC
dynamics and
microphysics**J. Reichardt et al.

[Title Page](#)[Abstract](#)[Introduction](#)[Conclusions](#)[References](#)[Tables](#)[Figures](#)[◀](#)[▶](#)[◀](#)[▶](#)[Back](#)[Close](#)[Full Screen / Esc](#)[Print Version](#)[Interactive Discussion](#)

© EGU 2003

from the observations is particularly difficult because no straightforward relationship exists between particle optical and particle microphysical properties, and because scattering information contained in the lidar data is limited to the backscattering direction. Another difficulty is that lidar data yield cloud geometrical and optical information that are convoluted in time and space. If PSC statistics are the research focus, this is not a serious limitation. However, if the life cycles of individual PSCs are to be investigated, this problem has to be addressed.

Mountain wave-induced PSCs constitute an ideal natural laboratory to investigate the formation and dissipation of cloud particles. Under quasi-stationary meteorological conditions these mesoscale clouds do not strongly vary their spatial position relative to the ground, and in the air flowing through them particles nucleate, grow, and evaporate continuously over a period of hours. Previously, particle evolution in wave PSCs was studied based on optical data acquired with airborne lidar instrumentation (Carslaw et al., 1998b; Tsias et al., 1999; Wirth et al., 1999; Dörnbrack et al., 2002; Hu et al., 2002; Fueglistaler et al., 2003). In these cases, the time-space convolution of the lidar data did not constitute a major problem for the analysis because the observation of quasi-localized PSCs can be regarded as taken at a fixed point in time if the lidar probes the cloud along a flight track parallel to the main horizontal wind direction. To our knowledge, a similar study that rests upon measurements with ground-based lidars has not been attempted so far, mainly because of the fact that this simplifying assumption cannot be made. In this contribution, such an analysis of wave PSC particle evolution is presented for the first time.

In winter 1996/7 the lidars of the GKSS Research Center (GKSS Raman lidar; Reichardt et al., 1996) and of the University of Bonn (U. Bonn lidar; Müller et al., 1997) were operated at Esrange as part of an international campaign dedicated to investigations of dynamically induced regional-scale PSCs in the lee of the Scandinavian mountains (Fricke, 1997). In the morning of 16 January 1997, increasing northwesterly tropospheric wind flow over the Scandinavian mountain ridge excited gravity waves propagating into the stratosphere and generating temperature minima eventually low

**Mountain wave PSC
dynamics and
microphysics**J. Reichardt et al.

[Title Page](#)[Abstract](#)[Introduction](#)[Conclusions](#)[References](#)[Tables](#)[Figures](#)[◀](#)[▶](#)[◀](#)[▶](#)[Back](#)[Close](#)[Full Screen / Esc](#)[Print Version](#)[Interactive Discussion](#)

© EGU 2003

enough for nucleation of solid particles. This mountain wave PSC event, possibly the strongest that winter (Dörnbrack et al., 2001), lasted the whole day until wave activity ceased in the evening. Because of favorable tropospheric weather conditions the two Esrange lidars could monitor the development of the quasi-stationary PSC system over its full life cycle. This unique data set is presented here, and an analysis in terms of PSC dynamics and microphysics is given. For the first time, a mesoscale model simulation is utilized to resolve the time-space ambiguity of ground-based lidar observations, and microphysical properties of crystalline PSC particles are retrieved assuming polyhedral, or spheroidal, particle shapes (Reichardt et al., 2002c).

The article is organized as follows. Section 2 is a description of the lidar instruments and of the measurement techniques used for the determination of the PSC optical properties. In Sect. 3, the meteorological situation on 16 January 1997 is discussed, and the results of the mesoscale model are presented. In Sect. 4, a macrophysical interpretation of the lidar observations is given that is based on the mesoscale numerical simulation and on the PSC optical characteristics. Section 5 focuses on the microphysical analysis of selected time periods during the PSC development. Section 6 is a summary.

2. Instrumentation and data analysis

The GKSS Raman lidar is a polarization Raman DIAL for nighttime measurements of clouds, water vapor (troposphere only), and ozone (Reichardt et al., 1996). In January 1997 this mobile system was operated at Esrange, the emitted laser wavelengths were 308 and 355 nm. PSC optical properties (including depolarization ratio) are determined at 355 nm. No effort was made to retrieve PSC properties at the shorter wavelength because absorption by ozone molecules poses a problem for the data analysis of thin PSCs here.

The U. Bonn lidar at Esrange is a polarization Raman lidar, operating at a wavelength of 532 nm at the time of the measurements discussed here. Daylight capabilities ex-

isted for the parallel-polarized elastic return signal (Müller et al., 1997).

Backscatter ratio R (ratio of total to molecular backscattering) is determined similarly with both instruments. The ratio of an elastic-backscatter lidar signal to the corresponding vibrational-rotational Raman signal (molecular nitrogen) is formed, and calibrated at heights with negligible particle scattering. It is important to note that although R is a useful parameter for studies of cloud dynamics and, together with depolarization ratio, PSC classification (Browell et al., 1990), it is less helpful in the determination of microphysical properties. Backscatter ratio is a relative measure that does not only contain information about the PSC, but also about the atmosphere. Furthermore, as discussed by Reichardt et al. (2002c), R cannot be utilized directly for retrieval of particle shapes and sizes because it depends on the particle number density. Instead we have used lidar optical properties, which are independent of the concentration of the PSC particles, and which therefore contain information about the scattering properties of the cloud particles alone. Specifically, these are the extinction-to-backscatter (lidar) ratio S_{par} and the particle depolarization ratio δ_{par} (subscript “par” denotes “particle”). Although combination of GKSS and U. Bonn lidar data measured at 355 and 532 nm would have allowed us to employ also the (number-density-independent) coefficients of the wavelength dependence of depolarization ratio and of backscattering coefficient in the microphysical retrieval, we have not done so. The reason is an inconsistency in our depolarization data. Particle depolarization ratios of the water-ice PSC observed in the afternoon of 16 January 1997 are overwhelmingly < 0.04 at 532 nm (Baumgarten, 1997), whereas δ_{par} values obtained with the GKSS Raman lidar are > 0.5 (see Fig. 7). This pronounced discrepancy cannot be explained by wavelength-dependent scattering by the presumably rather large ice particles. Because 355-nm depolarization ratios are calibrated without critical assumptions (see below) and, moreover, are in good agreement with theoretical optical properties of micron-size crystalline particles (see Fig. 8), only the measurements of the GKSS Raman lidar are considered for the microphysical interpretation of the PSC data. Use of the U. Bonn lidar observations is restricted to visualizing the development of the macrophysical PSC properties during

**Mountain wave PSC
dynamics and
microphysics**J. Reichardt et al.

[Title Page](#)[Abstract](#)[Introduction](#)[Conclusions](#)[References](#)[Tables](#)[Figures](#)[◀](#)[▶](#)[◀](#)[▶](#)[Back](#)[Close](#)[Full Screen / Esc](#)[Print Version](#)[Interactive Discussion](#)

daytime.

Particle depolarization ratios are determined by use of the conventional two-signal technique of [Schotland et al. \(1971\)](#), which is based on the assumption that the measured depolarization ratio is proportional to the ratio of two lidar signals sensitive to either perpendicular- or parallel-polarized light. Depolarization measurements with this technique have to be calibrated. In our case, this was done by fitting the depolarization-ratio profile obtained for the 16 January 1997 ice PSC between 16:55 and 17:55 UT to the one determined for the same time period with a new three-signal method for depolarization measurements ([Reichardt et al., 2003](#)). This approach to calibration is accurate because it is largely insensitive to experimental errors, and no critical assumptions about the atmospheric depolarization ratio at some reference height have to be made. Finally, to obtain δ_{par} , the calibrated polarization data are corrected for the influence of molecular scattering which depresses the measured depolarization ratio in optically thin PSCs and at cloud boundaries below the value of light scattered by the PSC particles alone. For a discussion of statistical and systematic errors see [Reichardt et al. \(2002a\)](#).

Height-resolved S_{par} data have proven valuable in microphysical studies of tropospheric clouds ([Reichardt et al., 2002b](#)), and show great potential in PSC investigations ([Reichardt et al., 2002c](#)). PSC lidar-ratio profiles, however, cannot be determined with the GKSS Raman lidar, because the Raman signal strength is not sufficient for the calculation of particle extinction coefficients above ~ 20 km. In order to have some S_{par} information available for the PSC under investigation, we calculate the PSC-layer mean value of S_{par} , \bar{S}_{par} , as PSC optical depth τ divided by integrated PSC backscatter coefficient. The latter is obtained from the backscatter-coefficient profile which is determined with the Raman-lidar technique ([Ansmann et al., 1992](#)). The optical depth of the PSC can be calculated according to

$$\tau = \ln[N(z_b)/N(z_t)]/2, \quad (1)$$

where $N(z_b)$ and $N(z_t)$ is the elastic lidar signal at heights below and above the PSC,

**Mountain wave PSC
dynamics and
microphysics**

J. Reichardt et al.

Title Page

Abstract

Introduction

Conclusions

References

Tables

Figures

◀

▶

◀

▶

Back

Close

Full Screen / Esc

Print Version

Interactive Discussion

Mountain wave PSC dynamics and microphysics

J. Reichardt et al.

Title Page

Abstract

Introduction

Conclusions

References

Tables

Figures

◀

▶

◀

▶

Back

Close

Full Screen / Esc

Print Version

Interactive Discussion

© EGU 2003

respectively. Before τ is calculated, N is corrected for background, range, and for backscattering and extinction by molecules. Radiosonde data of the measurement night are used to determine the atmospheric density profile required for the correction of molecular scattering. The residual, absolute systematic errors in \bar{S}_{par} that result from this Rayleigh correction are the larger the smaller the PSC optical depth. However, since the latter is often anticorrelated with lidar ratio (optically thin mountain wave PSCs consist of small particles with high S_{par}), the \bar{S}_{par} uncertainty can be estimated to be $\sim 20\%$ for all PSC measurements considered here. Obviously, \bar{S}_{par} is the more meaningful the smaller the altitude variations in particle optical, and hence microphysical, properties are. In our analysis we have used the other particle optical property measured, δ_{par} , as an indicator of PSC variability.

Recent analyses of lidar measurements suggest that scattering by both solid and liquid particles may contribute significantly to the optical properties of low- R (type-I, according to the classification of Browell et al., 1990) PSCs (e.g. Gobbi et al., 1998; Stein et al., 1999; Toon et al., 2000; Biele et al., 2001). In this case, the interpretation of the PSC data in terms of the two coexisting particle classes can be improved if backscatter coefficients (or backscatter ratios) are studied separately for both states of polarization, since droplet scattering adds to the parallel-polarized lidar signal alone (single scattering assumed) whereas the light backscattered from nonspherical solid particles has both parallel- and perpendicular-polarized components. Our discussion of the type-I PSCs on 16 January 1997 includes an analysis that is similar to these previous studies, but in order to avoid calibration problems we look at the two quantities B^{\parallel} and B^{\perp} , the ratios of, respectively, parallel-polarized and perpendicular-polarized particle backscatter coefficients to the backscatter coefficient of molecular scattering. B^{\parallel} and B^{\perp} are calculated from the R and δ_{par} measurements according to

$$B^{\parallel} = (R - 1)/(1 + \delta_{\text{par}}), \quad (2)$$

$$B^{\perp} = \delta_{\text{par}}(R - 1)/(1 + \delta_{\text{par}}). \quad (3)$$

**Mountain wave PSC
dynamics and
microphysics**

J. Reichardt et al.

[Title Page](#)[Abstract](#)[Introduction](#)[Conclusions](#)[References](#)[Tables](#)[Figures](#)[⏪](#)[⏩](#)[◀](#)[▶](#)[Back](#)[Close](#)[Full Screen / Esc](#)[Print Version](#)[Interactive Discussion](#)

© EGU 2003

Obviously, B^{\parallel} and B^{\perp} contain the same information as R and δ_{par} but some aspects of PSC scattering are easier discerned if one or the other pair of variables is used.

On 16 January 1997, optically thin tropospheric ice clouds were present above the lidar site, sporadically before and continuously after $\sim 20:00$ UT, respectively (Fricke et al., 1999). For that reason, the effect of multiple scattering in cirrus clouds on the PSC observations is briefly addressed in the following, since it might be seen as a possible source of error in the determination of PSC optical properties, particularly δ_{par} . We show that the multiple-scattering effect is negligible. We employed the multiple-scattering model described by Reichardt et al. (2000a) and Reichardt (2000) to simulate the multiple-scattering contributions to the elastic lidar return signals from the stratosphere. The cirrus extinction profile measured around 22:26 UT with the GKSS Raman lidar, and lidar parameters of this instrument were chosen for the simulations. Model results are shown in Fig. 1. Second-order scattering is the dominant multiple-scattering effect, it contributes $< \sim 4\%$ to the total lidar signal above 20 km. Since doubly scattered light experienced a single (direct) forward-scattering process in the cirrus cloud that does not change the state of polarization, this signal augmentation does not affect the depolarization measurement in PSCs. Only backscattered light of higher scattering orders (two or more scattering processes in the cirrus clouds) might interfere with the δ_{par} determination, however, they are irrelevant in our case (scattering orders > 2 amount to less than 0.2% above 20 km). Finally, we want to point out that multiple scattering in cirrus clouds does not play a role in measurements of PSC backscatter and lidar ratios either, because, respectively, the multiple-scattering contributions to elastic and Raman return signals cancel out (Wandinger, 1998), and the ratios of multiply to singly scattered light depend only weakly on height in the stratosphere.

3. Meteorological setting

Results of a mesoscale model simulation illustrate the meteorological setting. The mesoscale fields are calculated with the non-hydrostatic weather prediction model

**Mountain wave PSC
dynamics and
microphysics**

J. Reichardt et al.

Title Page

Abstract

Introduction

Conclusions

References

Tables

Figures

◀

▶

◀

▶

Back

Close

Full Screen / Esc

Print Version

Interactive Discussion

© EGU 2003

MM5-version 3.4 (Dudhia, 1993; Dudhia et al., 2001). The outer model domain is centered at (65° N, 20° E) with an extension of 2457 km × 2457 km. In this domain a horizontal grid size of $\Delta x = 27$ km is used. A local grid refinement scheme (nested domains of 9 and 3 km horizontal resolution, respectively) is applied to resolve most of the horizontal wavenumber spectrum of vertically propagating gravity waves excited by the orography.

The mesoscale simulation presented in this paper was performed with 128 vertical levels up to the model top at 10 hPa (~30 km) which results in a high spatial resolution of $\Delta z \approx 230$ m. More important for a correct modeling of the vertical propagation of mountain waves into the stratosphere, however, is the modified radiative top boundary condition of Zängl (2002) which is applied in the current MM5 version. This boundary condition reduces the reflection at the model top significantly (Dörnbrack et al., 2002). Radiative and moist processes are switched off since the prime concern lies in the dynamics of mountain waves at upper levels. The initial conditions and boundary values of the model integration were prescribed by 6-hourly operational analyses of the ECMWF model with a horizontal resolution of 0.5° in latitude and longitude and 15 pressure levels between the surface and the 10-hPa pressure level.

Figure 2 illustrates the simulated stratospheric temperature fields of the innermost model domain. Northern Scandinavia was located entirely inside the polar vortex on 16 January 1997. Inside the vortex the stratospheric temperature field at the isentropic surface $\Theta = 550$ K is rather uniform with $T \approx 192$ K (over the Norwegian Sea in the horizontal sections of Fig. 2). Vertically propagating mountain waves generate elongated stratospheric temperature anomalies parallel to the mountain ridge. As will be discussed later, hydrostatic gravity waves in the non-rotating regime with horizontal wavelengths ≤ 100 km lead to vertical displacements of isentropes directly above the mountain ridge (compare the vertical sections in Fig. 2) whereas longer hydrostatic gravity waves in the rotating regime propagate also leeward (we use the terminology of Gill, 1982). At $\Theta = 550$ K the local temperature deviates from the average temperature inside the polar vortex by up to 12 K. There are two dominating stratospheric

**Mountain wave PSC
dynamics and
microphysics**J. Reichardt et al.

[Title Page](#)[Abstract](#)[Introduction](#)[Conclusions](#)[References](#)[Tables](#)[Figures](#)[◀](#)[▶](#)[◀](#)[▶](#)[Back](#)[Close](#)[Full Screen / Esc](#)[Print Version](#)[Interactive Discussion](#)

© EGU 2003

temperature anomalies. At 00:00 UT, the horizontal distance between the westerly and the easterly one is about 150 km and increases to more than 400 km in the afternoon of 16 January 1997 (not within the display range of Fig. 2). Furthermore, the series of horizontal sections indicates an apparent downstream advection of the westerly cold anomaly towards the east. However, inspection of the vertical sections reveals that the horizontal wavelength of the westerly temperature anomaly increases from less than 50 km at 00:00 UT to about 200 km at 16:00 UT. Consequently, also its position relative to the mountain range shifts leeward. This is due to the excitation of hydrostatic gravity waves in the rotating regime by the long-lasting flow past the Scandinavian mountain ridge (e.g. Dörnbrack et al., 1999, 2002). These inertia-gravity waves have a non-vanishing horizontal component of the group velocity, therefore they are able to produce stratospheric temperature anomalies in the lee of the mountain ridge. Their smaller vertical group velocity compared to non-rotating hydrostatic waves lead to about 5 to 10 times larger propagation times to stratospheric levels and to an increasing distance between the westerly and easterly temperature minima during the day.

The coldest region inside the stratospheric temperature anomaly, however, propagates northward and is related to the position of the jetstream underneath. Figure 3 depicts the tropospheric meteorological evolution above the Scandinavian mountain range on 16 January 1997. The prominent features are the northward-tilted tropopause (the white band in the vertical sections corresponding to a potential vorticity (PV) value of 2 PVU) and the tropopause fold associated with a strong jetstream. The difference between the tropopause heights on the cyclonic and the anticyclonic side is about 6 km. The jetstream attains a maximum velocity of $\sim 60 \text{ ms}^{-1}$ in its core. In the course of time the tropopause fold and jetstream advance northward (see the horizontal sections of PV and wind on the 308-K isentropic surface). Near-surface winds upstream of Scandinavia are nearly perpendicular to the main mountain ridge. They peak at maximum values of $\sim 20 \text{ ms}^{-1}$ at 850 hPa between 00:00 UT and 12:00 UT and decrease afterwards significantly to values below 5 ms^{-1} (not shown). Hours later this weakening of

**Mountain wave PSC
dynamics and
microphysics**

J. Reichardt et al.

[Title Page](#)[Abstract](#)[Introduction](#)[Conclusions](#)[References](#)[Tables](#)[Figures](#)[◀](#)[▶](#)[◀](#)[▶](#)[Back](#)[Close](#)[Full Screen / Esc](#)[Print Version](#)[Interactive Discussion](#)

© EGU 2003

the near-surfaces winds causes the wave activity in the stratosphere to decrease and eventually cease (after $\sim 18:00$ UT, see Fig. 4).

The key to understanding the lidar observations at Esrangle and the associated stratospheric temperature structure lies in the position of the jetstream relative to the lidar site. The large vertical shear of the zonal wind U in the troposphere $\partial U / \partial z = 60 \text{ ms}^{-1} / 8000 \text{ m} = 7.5 \times 10^{-3} \text{ s}^{-1}$ generates a Froude number profile $\mathcal{F}(z) = \mathcal{N} h / U$ falling with altitude, where \mathcal{N} is the buoyancy frequency ($\sim 0.01 \text{ s}^{-1}$) and $h \approx 1500 \text{ m}$ is the height of the Scandinavian mountain ridge. In such regions, vertical gravity wave propagation is significantly facilitated. As a consequence, the strongest stratospheric cooling due to mountain waves is locked with the position of the jetstream advancing northward (see the stratospheric temperature anomaly in the vertical section of Fig. 3). The minimum temperature drops from 186 K (00:00 UT) to less than 182 K (16:00 UT) in the mountain wave-induced stratospheric temperature anomaly. In summary, the enhanced wave activity above the jetstream leads to an extra cold region in an altitude range between 22 and 26 km which proceeds northward while the longer horizontal mountain waves result in an eastward drift of the temperature anomaly.

4. PSC macrophysical properties

The stratospheric temperature field downstream the Scandinavian mountains can be best described as a series of temperature minima parallel to the ridge whereby the intensity of mountain wave cooling is modulated by synoptic-scale (jetstream dynamics) and mesoscale (wave propagation) processes (Fig. 2). As the result of the combined synoptic and mesoscale dynamics, the height versus time representation of the temperature above Esrangle resembles a distorted quadrupole field, with the 192-K isothermal lines being the center axes (Fig. 4). In the morning of 16 January 1997, stratospheric conditions at the lidar site are governed by the easterly mountain wave-induced temperature anomaly leading to temperatures warmer and colder than 192 K at heights below and above $\sim 23 \text{ km}$, respectively. Due to the long-lasting flow past the mountain

**Mountain wave PSC
dynamics and
microphysics**

J. Reichardt et al.

[Title Page](#)[Abstract](#)[Introduction](#)[Conclusions](#)[References](#)[Tables](#)[Figures](#)[◀](#)[▶](#)[◀](#)[▶](#)[Back](#)[Close](#)[Full Screen / Esc](#)[Print Version](#)[Interactive Discussion](#)

© EGU 2003

ridge and the associated dilatation of the horizontal wavelength this pattern reverses over time. At $\sim 07:00$ UT, the stratosphere between 21 and 27 km is nearly isothermal at $T = 192$ K. Later on, the intensifying westerly temperature anomaly dominates the temperature field over Esrange with temperatures colder below, and warmer above, the sloping 192-K isotherm.

The observed PSC evolution above Esrange is mostly related to the development of the westerly stratospheric temperature anomaly, only the isolated PSC patches detected at altitudes > 25 km in the early morning between 02:00 UT and 06:00 UT are probably generated at the windward edge of the easterly temperature minimum. The main PSC event, however, starts around 04:00 UT when first particle backscattering is measured at 23.5–24 km. Over the next 2 h the PSC cloud base lowers to minimum heights around 20.5 km. This correlates with a decrease in temperature at altitudes < 23 km. Afterwards, PSC base and top move steadily upwards by ~ 170 m/h until 19:30 UT with the geometrical thickness of the PSC remaining nearly constant at ~ 3 km. The simulated mountain wave-induced stratospheric anomaly also shows this upward propagation.

PSC optical data before 07:40 UT reveal a growth of R and a reduction of δ_{par} with decreasing temperature. The change is particularly pronounced at sunrise around 06:40 UT. This transition in PSC optical signature, which is discussed in greater detail in Sect. 5.1, suggests that scattering by liquid ternary aerosol (LTA) droplets increasingly dominates scattering by solid particles, most likely consisting of nitric acid trihydrate (NAT; the leading edge of the PSC follows quite well the NAT equilibrium temperature T_{NAT}).

After sunrise and until $\sim 17:00$ UT, R values continue to increase while the ambient air masses are cooling. Backscatter spikes at 24 km between 09:00 UT and 11:30 UT are probably caused by PSC patches consisting predominantly of ice particles (type-II PSC) rather than by LTA droplets (type-Ib PSC) or crystalline NAT particles (type-Ia PSC) because R values clearly exceed those expected for type-I PSCs. If this interpretation was correct, we would have observed ice particles that were nucleated

**Mountain wave PSC
dynamics and
microphysics**J. Reichardt et al.

[Title Page](#)[Abstract](#)[Introduction](#)[Conclusions](#)[References](#)[Tables](#)[Figures](#)[◀](#)[▶](#)[◀](#)[▶](#)[Back](#)[Close](#)[Full Screen / Esc](#)[Print Version](#)[Interactive Discussion](#)

© EGU 2003

previously in the core of the westerly temperature minimum ~ 80 km upstream and that survived advection to the lidar site in subsaturated air (temperatures are several degrees Kelvin above the ice equilibrium temperature T_{ice}), albeit evaporating. The hypothesis of subliming ice particles being the cause for the backscatter maxima before 11:30 UT is supported by the observation of a PSC region with even larger R values entering the lidar field of view around noon at similar heights in air masses still warmer than T_{ice} , that increases in vertical extent to both lower and higher altitudes over time while the stratosphere below 26 km is cooling until T_{ice} is reached around 13:00 UT.

Between 13:00 UT and $\sim 18:00$ UT the cold core of the westerly temperature anomaly resides directly above Esrange. The mesoscale simulation indicates minimum temperatures of 181 K at 24 km which is about 3 K below the frost point. Therefore one can conclude that the extreme backscatter ratios (> 25 at 355 nm, > 150 at 532 nm) and particle depolarization ratios (> 0.5) measured by the two lidars are the optical signature of a PSC II in the early stages of its life cycle with possibly newly nucleated, and growing ice particles.

After 18:00 UT wave activity weakens leading to an upstream shift of the attenuating temperature minimum. The Esrange lidars monitor the outflow of the westerly temperature anomaly again. Around 19:00 UT the PSC collapses to a 0.5-km wide layer. Associated with the change in geometrical properties is a drastic transition in PSC backscatter and particle depolarization ratios. The slowly subsiding thin PSC clearly exhibits the optical characteristics of a PSC Ib (LTA droplets), except for short-lived patches around 20:00 UT with elevated δ_{par} . Apparently, the windward temperature minimum shallowed to such an extent that nucleation of solid particles is significantly reduced. Wave-processing foremost results in growth and evaporation of the liquid aerosol. These droplets may have originated from the synoptic PSC I that was observed at the same time at similar heights on the weather side of the Scandinavian mountain ridge over the research facility ALOMAR approximately upwind Esrange (Fricke et al., 1999). The transition from PSC II to PSC Ib as observed between 17:00 UT and 20:00 UT over Esrange will be discussed in more detail in Sect. 5.2.

**Mountain wave PSC
dynamics and
microphysics**J. Reichardt et al.

[Title Page](#)[Abstract](#)[Introduction](#)[Conclusions](#)[References](#)[Tables](#)[Figures](#)[◀](#)[▶](#)[◀](#)[▶](#)[Back](#)[Close](#)[Full Screen / Esc](#)[Print Version](#)[Interactive Discussion](#)

© EGU 2003

In summary, the following interpretation of our ground-based lidar measurements in terms of temporal evolution of the PSC can be given. The dominant mountain wave-induced temperature anomaly develops first upwind and then above Esrang. In the morning and until the early afternoon while wave activity intensifies and horizontal wavelength increases, the quasi-stationary PSC extends into the field of view (trailing edge first), thus leading to a time-reversed observation of PSC evolution: later stages of particle history are observed before earlier stages. First, NAT particles are detected as the outflow from the westerly wave-induced PSC at relatively warm temperatures (all LTA droplets or ice particles are evaporated). Then, as the cold core of the wave expands eastward (due to wave dynamics) and northward (due to jetstream dynamics), more and more LTA droplets and, after 09:00 UT, ice particles appear above the lidar site, causing the PSC optical signature to change from PSC Ia over PSC Ib to PSC II. The earliest stage of PSC particle history is observed around 17:00 UT when ice particles are nucleated directly above Esrang. Later on, as the wavelength shortens and the temperature anomaly moves westward again, lidar measurements are in sync with the temporal PSC particle evolution: earlier stages are observed before later stages. The microphysical analysis in Sect. 5.3 shows that the retrieved ice particle sizes decrease with time, probably due to a diminishing growth rate and eventually evaporation. With the cessation of particle nucleation upwind, the major mountain wave PSC event over Esrang comes to an abrupt end. All that remains is a wave-processed synoptic PSC Ib that is observed until lidar operation is ended at 03:10 UT on 17 January 1997.

Interestingly, the wave PSC as monitored above Esrang does neither exhibit a laminated vertical structure nor a temporal or spatial oscillatory pattern which are common features of this PSC type otherwise when observed with airborne lidars (e.g. Wirth et al., 1999; Dörnbrack et al., 2002). Given the meteorological setting on 16 January 1997, it is probable though that similar features would have been detected if there had been a lidar-equipped aircraft observing the PSC along a flight track parallel to the main tropospheric wind direction (e.g. with a ground track similar to the base of the vertical section of Fig. 2).

5. PSC microphysical properties

In this section we present the results of our microphysical studies that helped us derive the general interpretation of our lidar measurements on 16 January 1997 given before. It has to be pointed out, however, that a full assessment of PSC microphysics cannot be expected from our analysis. The relation between PSC microphysical and optical properties is complicated. In previous studies of PSC measurements acquired with airborne lidars, coupled optical and microphysical modeling was employed to counter this problem (e.g. Carslaw et al., 1998b; Wirth et al., 1999). The success of this approach is in part due to the relatively simple observation geometry of the measurements, as explained before. In order to apply this technique to PSC measurements with ground-based lidar instruments, however, one would have to take into account the time-space convolution of the observation which would require coupling of optical, microphysical and, additionally, dynamical models. Currently, such an extensive model is not available to us.

In our discussion we focus on the two major events that were captured with the GKSS Raman lidar, specifically, these are the transitions in the PSC optical characteristics from PSC Ia (with enhanced R) to PSC Ib (04:00–09:00 UT), and from PSC II to PSC Ib (17:00–20:00 UT).

5.1. PSC observations in the morning of 16 January 1997

Figure 5 displays the evolution of the PSC backscatter-ratio and depolarization-ratio profiles in the morning of 16 January 1997. To increase the precision of the \bar{S}_{par} determination, lidar data are summed over three consecutive measurement intervals M1–M3 with relatively little variation in PSC optical and geometrical properties. Generally, δ_{par} and \bar{S}_{par} decrease, and R increases, with time although some exceptions exist. For example, cloud-base δ_{par} values measured during interval M3 are similar to those observed during interval M2. Apparently, LTA droplets that depress δ_{par} at the PSC altitudes above are smaller in number, small in size, or completely absent here. In-

Title Page

Abstract

Introduction

Conclusions

References

Tables

Figures

◀

▶

◀

▶

Back

Close

Full Screen / Esc

Print Version

Interactive Discussion

**Mountain wave PSC
dynamics and
microphysics**

J. Reichardt et al.

terestingly, \bar{S}_{par} values of intervals M2 and M3 are comparable despite the significant change in the fractional contributions of crystalline and liquid particles to PSC light scattering (see Fig. 6). It is possible that opposing trends in the temporal development of solid-particle and droplet S_{par} simply cancel out, however, as we will discuss later, decomposition of the PSC optical signature into particle-type specific optical properties as well as microphysical considerations suggest instead that the solid and liquid particles present have similar lidar ratios that change little over time.

To facilitate interpretation of the lidar measurements, backward trajectories based on mesoscale simulation fields were calculated. Air parcel temperature histories are presented in Fig. 5 for selected PSC heights. Only the last 2 h prior to the lidar observations are shown. The mountain wave induced several cycles of cooling and heating of which, in the case of the main PSC layer between 20 and 25 km, the most pronounced occurred 30 min before the observations. In this temperature anomaly of rather short duration, the air masses are cooled by several degrees Kelvin to minimum temperatures with high cooling rates (particularly during measurements M2 and M3 at heights < 23 km), but fail to reach in all but one case (22.5 km, measurement M3) temperatures 3–4 K below the frost point (assuming 5 ppmv H₂O) which is generally regarded as the threshold temperature range for solid-particle nucleation (Tabazadeh et al., 1997; Carslaw et al., 1998b).

Since the question whether or not temperatures dropped sufficiently to allow ice particles to form is important for understanding the PSC event over Esrange, it has to be carefully addressed. Several explanations are conceivable. First, the simulated mesoscale minimum temperatures are accurate and the assumed water vapor content is about right. This would mean that indeed no solid particles nucleated in the mountain wave. Particle depolarization ratios measured during measurements M1–M3 would be due to solid particles already present upwind the Scandinavian mountain ridge that served as condensation nuclei while being transported through the temperature anomaly. According to synoptic-scale trajectory calculations based on the operational ECMWF analyses (not shown), the air parcels detected at 30 hPa crossed

[Title Page](#)[Abstract](#)[Introduction](#)[Conclusions](#)[References](#)[Tables](#)[Figures](#)[◀](#)[▶](#)[◀](#)[▶](#)[Back](#)[Close](#)[Full Screen / Esc](#)[Print Version](#)[Interactive Discussion](#)

© EGU 2003

**Mountain wave PSC
dynamics and
microphysics**

J. Reichardt et al.

Title Page

Abstract

Introduction

Conclusions

References

Tables

Figures

◀

▶

◀

▶

Back

Close

Full Screen / Esc

Print Version

Interactive Discussion

© EGU 2003

the southern tip of Greenland 24 h before the measurements, and maintained temperatures $< T_{\text{NAT}}$ afterwards. Hence it is possible that the advected air was processed in a mountain wave over Greenland at that earlier time (Carslaw et al., 1998a), and that solid condensation nuclei preexisted. Second, the temperature simulations are correct, but stratospheric humidity is underestimated. If the water vapor concentration was, e.g. about 7 ppmv rather than 5 ppmv, T_{ice} would rise by ~ 1.5 K increasing the likelihood of ice particle nucleation significantly. Third, simulated mesoscale temperatures are too warm. In the morning of 16 January 1997, this effect would be aggravated if the small-scale structure of the temperature anomaly were not fully resolved by the model. The studies of Larsen et al. (2002) and Fueglistaler et al. (2003) show that the discrepancies between simulated and measured temperatures can be several degrees Kelvin, with the mesoscale model temperatures consistently being warmer. In our case, a temperature correction of -1 to -3 K (depending on height) would be required to trigger ice nucleation both in the morning (Fig. 5) and the afternoon (Fig. 7) of 16 January (all other parameters unchanged), which is in the range of temperature corrections Larsen et al. (2002) had to apply to match microphysical simulations and observations. The assessment that model temperatures may be too warm is corroborated by the observation of large amounts of LTA above 22 km in measurement interval M3. Our model simulations yield temperatures within 1 K below T_{NAT} in the LTA layer, while the theoretical work of Carslaw et al. (1994) on equilibrium growth of liquid aerosol show that LTA volume does not increase significantly unless temperatures fall several degrees Kelvin below T_{NAT} . In summary, in view of the accuracy of the mesoscale numerical simulations and the uncertainties associated with the stratospheric trace gas concentrations, we consider it very likely that mountain wave temperatures actually fell below the nucleation threshold of ice particles, and that solid particles subsequently formed. Preexisting solid particles may have aided PSC formation as additional condensation nuclei.

As discussed previously, the transition in PSC optical properties observed in measurements M1–M3 is the result of changes in the size distributions of the coexisting

Mountain wave PSC dynamics and microphysics

J. Reichardt et al.

Title Page

Abstract

Introduction

Conclusions

References

Tables

Figures

◀

▶

◀

▶

Back

Close

Full Screen / Esc

Print Version

Interactive Discussion

© EGU 2003

solid and liquid particles. The main cause is the decrease in temperature in general, and above Esrange in particular, with time, allowing the LTA droplets to grow to larger volume in the mountain wave, and to maintain larger sizes during their subsequent advection to the lidar site (Fig. 5). The different trends in the evolution of the two particle types are visible in the ratios of polarized particle backscatter coefficients to molecular backscatter coefficient (Fig. 6). B^{\parallel} indicates the significant temperature-related increase in droplet volume while, in contrast, B^{\perp} exhibits little variability. From the spatial and temporal homogeneity of B^{\perp} the important conclusion can be drawn that the optical and microphysical properties of the crystalline particles are similar throughout the vertical extent of the PSC and remain unchanged during measurement intervals M1–M3. Consequently, the most accurate measurement of the depolarization ratio of scattering by these solid particles, $\delta_{\text{par}}^{\text{solid}}$, is obtained at heights and times where temperatures are too warm for liquid particles to exist in significant amounts. This condition should be approximately met in measurement M1, and we obtain $\delta_{\text{par}}^{\text{solid}} = 0.3 \pm 0.05$. With this estimate we are able to calculate the contributions of solid and liquid particles to the PSC backscatter ratio. Using the defining equations of B^{\perp} , B^{\parallel} , and $\delta_{\text{par}}^{\text{solid}}$ ($\delta_{\text{par}}^{\text{liquid}} = 0$), we obtain

$$(R - 1)_{\text{solid}} = B^{\perp} (1 + 1/\delta_{\text{par}}^{\text{solid}}), \quad (4)$$

$$(R - 1)_{\text{liquid}} = B^{\parallel} - B^{\perp} / \delta_{\text{par}}^{\text{solid}}, \quad (5)$$

with $R - 1 = (R - 1)_{\text{solid}} + (R - 1)_{\text{liquid}}$. The results of the computations are shown in Fig. 6. Solid-particle scattering dominates measurements M1 and M2; the low $(R - 1)_{\text{liquid}}$ values may either indicate scattering by few or small coexisting LTA droplets, or be the residual of our computations if $\delta_{\text{par}}^{\text{solid}}$ was overestimated. In contrast, $(R - 1)_{\text{liquid}} \gg (R - 1)_{\text{solid}}$ is found in measurement M3 for heights > 22 km. Interestingly, heights of highest $(R - 1)_{\text{liquid}}$ values and maximum HNO_3 concentrations coincide (Fig. 6).

We mentioned before that \bar{S}_{par} values of measurements M2 and M3 are similar. Since our trend analysis suggests that the optical properties of the solid particles re-

**Mountain wave PSC
dynamics and
microphysics**

J. Reichardt et al.

Title Page

Abstract

Introduction

Conclusions

References

Tables

Figures

◀

▶

◀

▶

Back

Close

Full Screen / Esc

Print Version

Interactive Discussion

main the same, this must also be the case for the LTA droplets, despite the fact that a significant size change occurred from one measurement to the other. Surprising as it first may sound, this finding can be explained if an increase in the refractive index of the droplets upon evaporation is taken into account (Sect. 5.3). For this reason, we will assume $S_{\text{par}} = (70 \pm 14)$ sr (20% systematic error, see Sect. 2) for both crystalline PSC particles ($\delta_{\text{par}}^{\text{solid}} = 0.25\text{--}0.35$, measurements M1–M3) and liquid PSC particles ($\delta_{\text{par}}^{\text{liquid}} = 0$, measurement M3) in our retrieval of microphysical properties. The elevated \bar{S}_{par} value measured during time period M1 is not considered representative of the solid particles, since the appearance of an isolated and short-lived PSC patch around 25.5 km (Figs. 4 and 5) might affect the accuracy of the \bar{S}_{par} measurement for the main PSC layer.

While it is straightforward to assume that the liquid particles consist of aqueous solution of HNO_3 and H_2SO_4 (LTA), the composition of the solid PSC particles is not that obvious. If ice particles grew to large sizes in the cold core of the mountain wave, it appears possible that these particles survived transport in subsaturated air until they were detected above Esrange after 30 min, although the heating rates were very high. However, if this hypothesis were true one would expect to see a correlation between B^\pm and the temporal evolution of the temperature profile, which is not observed. Therefore we assume that the solid particles consisted of NAT, although hydrates with higher $\text{H}_2\text{O}:\text{HNO}_3$ molar ratio might have been present also (Marti and Mauersberger, 1993). We would like to point out, however, that in situ data generally confirm the existence of NAT particles in the stratosphere (Fahey et al., 1989; Kawa et al., 1992; Voigt et al., 2000), in one measurement case that is similar to ours about 2 h downwind mountain wave-induced solid-particle nucleation (Voigt et al., 2000; Larsen et al., 2002; Dörnbrack et al., 2002; Schreiner et al., 2002).

5.2. PSC observations in the afternoon of 16 January 1997

Figure 7 shows our PSC measurements during and shortly after the core of the mountain wave-induced temperature anomaly resided over Esrange. PSC optical signatures are remarkably different from those observed earlier (Fig. 5). During measurements M4 and M5, R and δ_{par} reach maximum values of, respectively, 10–20 and 0.5–0.65, while $\overline{S}_{\text{par}}$ decreases to 20–35 sr. These optical characteristics, which are similar to those of cirrus clouds (Reichardt et al., 2002a), leave no doubt that the PSC consisted of large water-ice particles (PSC type II). Concurrent lidar measurements upwind Esrange on the weather side of the Scandinavian mountains reveal the existence of only a weak PSC (at 24 km, $R < 2$ at 532 nm; Fricke et al., 1999), which implies that the ice particles formed on their way between both sites. The temperature histories confirm cooling of the advected air masses of up to 15 K. Considering our discussion of temperature errors in Sect. 5.1, it thus seems probable that the temperatures got cold enough for ice-particle nucleation, and that the lidars at Esrange were actually monitoring this process during time periods M4 and M5 in the main PSC layer. Below 24.2 km during measurement M5, however, the meteorological conditions must have been different since R and δ_{par} are significantly smaller. The δ_{par} values of 0.05–0.1 may result from scattering by predominant LTA droplets that are in coexistence with either pre-existing solid particles, or a small number of ice particles nucleated but in the largest supercooled droplets.

Considering measurement M6, we favor the latter interpretation. Here maximum supercooling with respect to ice and the PSC optical properties of the main layer around 25 km are comparable to those of observation M5 at ~ 23.5 km. At these lower heights, however, no $\delta_{\text{par}} > 0$ is detected during measurement M6, indicating that a slight warming of ~ 1 K (compared to the temperature data of observation M5 at 23.5 km) is sufficient to suppress depolarization. This would not have been the case if solid particles had existed upwind the mountain wave.

Since in measurements M4–M6 scattering by either solid or liquid particles domi-

Title Page

Abstract

Introduction

Conclusions

References

Tables

Figures

◀

▶

◀

▶

Back

Close

Full Screen / Esc

Print Version

Interactive Discussion

nates, analysis of B^{\perp} and B^{\parallel} does not yield any additional information and is, therefore, not shown. Finally, we would like to point out that the modeled cooling rates of measurements M4–M6 are significantly lower (in absolute values) than those of measurements M1–M3. For that reason, it can be expected that the number density of nucleated ice and NAT particles is lower in the afternoon than in the morning because a smaller fraction of the population of supercooled droplets can freeze (Larsen et al., 2002; Fueglistaler et al., 2003).

5.3. Microphysical retrieval

In the following, PSC microphysical properties retrieved from the lidar measurements are discussed. The analysis first focuses on solid particles, specifically those observed during measurement intervals M1–M3, M4 and M5.

Estimates of particle shapes, sizes, and number concentrations are obtained by comparing measurements and theoretical optical data. For the first time S_{par} is used in the retrieval next to δ_{par} . Lidar ratio and particle depolarization ratio are two optical properties that ideally complement one another because they contain different information about the scattering matrix of the PSC particle ensemble. Both are independent of the particle number concentration and thus can be directly used to infer particle microphysical characteristics. Different principal particle shapes are investigated. Studies by Liu and Mishchenko (2001) and Reichardt et al. (2002c) demonstrate that retrieval results depend strongly on the assumed shapes of the particles, but to our knowledge PSC observations with lidar were analyzed by use of a spheroidal particle model only (Carslaw et al., 1998b; Tsias et al., 1999; Wirth et al., 1999; Flentje et al., 2002; Hu et al., 2002; Fueglistaler et al., 2003). In this study we compare the lidar data to the optical properties of spheroids, hexagons, and, for the first time, particles without any symmetry (irregular particles). It is assumed that the size distribution of the optically relevant PSC particles is narrow. In the case of mountain wave PSCs this approximation is justified as in situ measurements (Voigt et al., 2000), microphysical modeling

Title Page

Abstract

Introduction

Conclusions

References

Tables

Figures

◀

▶

◀

▶

Back

Close

Full Screen / Esc

Print Version

Interactive Discussion

(Tsias et al., 1999; Larsen et al., 2002), and size-spectrum-resolved retrievals from lidar data (Tsias et al., 1999; Wirth et al., 1999; Toon et al., 2000; Hu et al., 2002) confirm. Lidar measurements at multiple wavelengths are not available (see Sect. 2), therefore color ratio cannot be included in our analysis.

5 Solid particles are assumed to consist of NAT, or ice. For NAT a refractive index of 1.53 as observed by Deshler et al. (2000) is chosen, for ice the data of Warren (1984) are used (refractive index of 1.32 at 355 nm). Phase matrices of hexagons and irregular particles are calculated with the finite-difference time-domain method described by Yang et al. (2000). Scattering properties of spheroids with aspect ratios (defined as the ratio of length to diameter of the particle) smaller or larger than one are calculated according to the T-matrix technique (Waterman, 1970). The computer code used is available at http://www.giss.nasa.gov/~crmim/t_matrix.html (Mishchenko, 1991). Mie theory is applied to determine the phase functions of spheres (van de Hulst, 1981). For a discussion of the optical constants selected, and for more details about the computations see Reichardt et al. (2002c).

15 Figure 8 compares measured and theoretical optical properties of solid PSC particles. Theoretical lidar ratio and particle depolarization ratio are plotted versus the maximum dimension of the particles. Measurements are visualized with solid horizontal lines. In the case of δ_{par} , the line thickness reflects the variability of the observed PSC profile. Dashed horizontal lines show estimated systematic errors of S_{par} . Lengths and positions of the horizontal lines indicate particle size ranges with best-possible agreement between observations and theoretical data. The size ranges are relatively well defined in most cases, despite the fact that only two optical properties are available to constrain the retrieval. The reason for the stability of the solutions is the opposite dependence of δ_{par} and S_{par} on particle maximum dimension. Only if the particles are much larger than the observation wavelength, as it is the case in measurements M4 and possibly in M5, S_{par} and δ_{par} are not sensitive to changes in particle size any more, and the retrieval results become unstable.

25 For the solid particles observed during measurement intervals M1–M3 best agree-

Mountain wave PSC dynamics and microphysics

J. Reichardt et al.

Title Page

Abstract

Introduction

Conclusions

References

Tables

Figures

◀

▶

◀

▶

Back

Close

Full Screen / Esc

Print Version

Interactive Discussion

**Mountain wave PSC
dynamics and
microphysics**

J. Reichardt et al.

Title Page

Abstract

Introduction

Conclusions

References

Tables

Figures

◀

▶

◀

▶

Back

Close

Full Screen / Esc

Print Version

Interactive Discussion

© EGU 2003

ment between measured and theoretical optical data is found for irregular NAT and hexagonal ice particles. Nevertheless we can exclude the ice particles from our analysis if we take into account that in the morning of 16 January ambient temperatures were significantly warmer than T_{ice} , and that a well developed hexagonal symmetry is rather unlikely for small ice particles with 0.8–1.4 μm maximum dimension anyway. Examining the optical data of irregular NAT particles closer, we find that the particles most likely had maximum dimensions between 0.7 and 0.9 μm and aspect ratios between 0.75 and 1.25 or sizes of about 1.1 μm with either small (0.5) or large (1.5) aspect ratios. However, these latter particles can be discarded because their aspect ratios should be too extreme for micron-size particles.

From $(R - 1)_{\text{solid}} \approx 0.3$ it then follows that the particle number density was $n_{\text{NAT}} = 8 - 12 \text{ cm}^{-3}$, and that condensation of gas-phase HNO_3 was equivalent to 4.5–7.6 ppbv which was 31–55% of the total amount of available HNO_3 (generally, retrieval results are such that small maximum dimensions correspond to high number densities and small amounts of condensed HNO_3 , and vice versa). A summary of all measured optical and retrieved microphysical properties is given in Table 1.

The retrieval results are consistent with those of previous studies of solid-particle PSCs downwind mountain waves. Toon et al. (2000) infer from dual-wavelength polarization lidar data of Arctic PSCs high number densities (comparable to those of the condensation nuclei n_{CN}) of NAT particles $< 1 \mu\text{m}$, leading to a depletion of the gas-phase HNO_3 reservoir. Coupled microphysical and spheroid model-based optical modeling was performed by Carslaw et al. (1998b), Tsias et al. (1999), and Wirth et al. (1999). Comparison with the results of the latter investigation is particularly instructive, because the PSC event studied is similar to our 16 January 1997 observation regarding the location of the NAT PSC in close proximity to the upwind ice PSC, and the high cooling rates. Wirth et al. (1999) report particle sizes of 0.6–0.7 μm which is in agreement with our analysis for NAT spheroids (see Fig. 8), but which is smaller than our final retrieval results obtained for irregular NAT particles. This finding nicely illustrates the dependence of any microphysical retrieval on particle shape assumptions.

**Mountain wave PSC
dynamics and
microphysics**

J. Reichardt et al.

Title Page

Abstract

Introduction

Conclusions

References

Tables

Figures

◀

▶

◀

▶

Back

Close

Full Screen / Esc

Print Version

Interactive Discussion

© EGU 2003

Cooling rates and number densities of nucleated NAT particles seem to be correlated. In our case, maximum cooling rate at PSC center is 113 K/h (measurement M3) and $n_{\text{NAT}} = 8\text{--}12\text{ cm}^{-3}$, Wirth et al. (1999) report cooling rates of up to 60 K/h and $n_{\text{NAT}} = 3\text{--}6\text{ cm}^{-3}$, while Carslaw et al. (1998b) find much less particles per volume in the outflow of the mountain wave PSC with cooling significantly less rapid (Wirth et al., 1999). Recent in situ measurements (Voigt et al., 2003) as well as mesoscale/microphysical modeling (Fueglistaler et al., 2003) of mountain wave PSCs yield a similar dependence of n_{NAT} on cooling rate. Finally, Tsias et al. (1999) obtain NAT particle sizes $< 1\text{ }\mu\text{m}$ which is consistent with our analysis.

M4 and M5 observations are compared to theoretical optical data of ice crystals only, since the elevated backscatter ratios are too high for PSCs consisting of NAT particles, even for those generated by mountain waves (Tsias et al., 1999; Reichardt et al., 2000b). M4 depolarization ratios agree well with δ_{par} values of irregular ice particles $> 1.9\text{ }\mu\text{m}$, but measured lidar ratios are smaller than the theoretical data, even for a particle maximum dimension of $2.7\text{ }\mu\text{m}$. If a hexagonal particle shape is assumed, M4 measurements do not fit the FDTD results for particle sizes $< 2.7\text{ }\mu\text{m}$, but are close to the theoretical values obtained in the geometrical-optics approximation for columnar hexagons with aspect ratios between 1 and 2.5. This similarity implies that the particles observed during measurement interval M4 were large, probably $\gg 3\text{ }\mu\text{m}$. Since only a lower limit of the particle size can be given, particle number concentration can only be estimated. If n_{ice} were 5 and 10 cm^{-3} as retrieved by Hu et al. (2002) and Fueglistaler et al. (2003), the corresponding particle sizes would be, respectively, 4.3 and $3\text{ }\mu\text{m}$ for irregular, and 2.8 and $2\text{ }\mu\text{m}$ for hexagonal ice particles. Of these, only the $4.3\text{-}\mu\text{m}$ irregular particles appear to be consistent with the optical data which leads us to the conclusion that n_{ice} must have been $\leq 5\text{ cm}^{-3}$.

In the case of measurement M5, observation and theory are in excellent agreement for isometric and slightly oblate irregular ice particles (aspect ratios of 0.75 and 1) with sizes $> 1.9\text{ }\mu\text{m}$. Theoretical S_{par} values of hexagons indicate similar particle maximum dimensions, yet measured and calculated δ_{par} disagree. Again, the upper boundary of

**Mountain wave PSC
dynamics and
microphysics**

J. Reichardt et al.

Title Page

Abstract

Introduction

Conclusions

References

Tables

Figures

◀

▶

◀

▶

Back

Close

Full Screen / Esc

Print Version

Interactive Discussion

© EGU 2003

the particle size range cannot be retrieved because our observation at 355 nm are lacking sensitivity to size for large particles. For a more accurate size estimate, observations at longer wavelengths would be needed. The lower limit of the particle maximum dimension ($> 1.9 \mu\text{m}$) confines the particle number density to $n_{\text{ice}} < 27 \text{cm}^{-3}$. This upper boundary is probably too high for two reasons. First, n_{ice} should not be larger than the number concentration of the background aerosol, but maximum n_{CN} values measured in (mountain wave) PSCs are, to our knowledge, about 20cm^{-3} (Larsen et al., 2002). Second, our retrieval yields smaller particle number densities for all other measurement intervals. Contrarily, assuming a concentration of the ice particles similar to the estimated number densities of the NAT (M1–M3) and the LTA (M3, M6) particles ($n_{\text{ice}} = 8\text{--}11 \text{cm}^{-3}$, Table 1) and assuming an irregular isometric shape, we retrieve particle sizes in the range of 3 to $3.5 \mu\text{m}$ which are likely to be consistent with the PSC optical properties of measurement M5.

Assuming spheroidal particle shapes, we retrieve a mixture of slightly oblate and prolate particles (aspect ratios of 0.75 and 1.25) for the PSC observed during measurement M4. In the case of observation M5 the agreement between theoretical and observed data is rather poor. In contrast to the results obtained for irregularly shaped crystals and hexagons, the spheroidal particle model yields both lower and upper bounds of particle size and concentration for measurements M4 and M5. However, the retrieved particle sizes ($< 2.2 \mu\text{m}$) appear somewhat small for ice PSCs.

Finally, we analyze measurement M6 because, in theory, the optical signature of this PSC ($\delta_{\text{par}} < 5\%$, $S_{\text{par}} = 113 \text{sr}$) could stem from scattering by solid particles alone. Independently of particle composition and shape, observed and calculated optical properties agree well for particle maximum dimensions between 0.2 and $0.5 \mu\text{m}$. However, to explain the backscatter ratio of 1.7 with these small particles, one would have to assume number concentrations that are not realistic ($n_{\text{ice}} > 150 \text{cm}^{-3}$, $n_{\text{NAT}} > 65 \text{cm}^{-3}$). Thus we conclude that during measurement interval M6 solid and liquid PSC particles coexisted, and that LTA droplets dominated light scattering.

Figure 9 compares M3 and M6 lidar-ratio measurements of liquid PSC particles with

**Mountain wave PSC
dynamics and
microphysics**J. Reichardt et al.

[Title Page](#)[Abstract](#)[Introduction](#)[Conclusions](#)[References](#)[Tables](#)[Figures](#)[◀](#)[▶](#)[◀](#)[▶](#)[Back](#)[Close](#)[Full Screen / Esc](#)[Print Version](#)[Interactive Discussion](#)

© EGU 2003

355-nm theoretical data. Different chemical compositions of the LTA droplets were assumed in the Mie computations. In the stratosphere, an increase in temperature is related to a decrease in the water contents of the ternary solution and, thus, to an increase in LTA refractive index. In the UV it varies between 1.37 (85 wt% H₂O, $T \approx T_{\text{ice}} - 4 \text{ K}$) and 1.45 (55 wt% H₂O, $T \approx T_{\text{ice}} + 3 \text{ K}$) (Carslaw et al., 1994; Luo et al., 1996).

It is important to note that refractive indices between 1.39 and 1.53 correspond to diameters between 0.85 and 0.35 μm, respectively, for an assumed lidar ratio of 70 sr. Therefore it seems possible that the lidar ratio of a population of LTA droplets evaporating due to warming temperatures remains relatively unchanged, as we assumed to explain the almost identical S_{par} values of measurement intervals M2 and M3.

The optical data also show that the refractive index of the LTA droplets was smaller in measurement M6 than during the earlier observation M3, which is in accordance with the mesoscale numerical simulation of colder PSC temperatures for the afternoon. The relatively high backscatter ratios of 1.6–1.7 in both cases require the droplets sizes to be large since otherwise droplet concentrations would be too high. Considering temperature and R values, we infer an LTA refractive index of 1.39, droplet diameters of 0.7–0.9 μm, and particle concentrations of 7–11 cm⁻³ for measurement M3. These values correspond with condensation of 3.7–4.8 ppbv HNO₃ out of the gas phase. Combining the results of our microphysical retrieval for LTA and NAT particles, we obtain a total particle number density of 15–23 cm⁻³. Given the high stratospheric cooling rates in the morning of 16 January 1997, it appears likely that about all of the supercooled droplets nucleated ice particles in the mountain wave upwind Esrange, which would mean that on ~ 53% of these particles ice-mediated nucleation of NAT occurred (the remaining ~ 47% of the ice particles released liquid droplets after ice evaporation). Wirth et al. (1999) report a similar fraction for a mountain wave PSC with comparable cooling rates. The total amount of condensed HNO₃ sums up to 8.2 to 12.4 ppbv, i.e. 57–90% of the HNO₃ gas reservoir. This compares well with the microphysical model results obtained for the mountain wave PSC studied by Voigt et al. (2000); Larsen et

**Mountain wave PSC
dynamics and
microphysics**

J. Reichardt et al.

Title Page

Abstract

Introduction

Conclusions

References

Tables

Figures

◀

▶

◀

▶

Back

Close

Full Screen / Esc

Print Version

Interactive Discussion

© EGU 2003

al. (2002); Dörnbrack et al. (2002); Schreiner et al. (2002). According to Larsen et al. (2002), depletion of the HNO_3 gas reservoir can reach 100% in the ice PSC, and decreases downwind. About 1 h after the air parcels warmed up to temperatures $> T_{\text{ice}}$, depletion between 40% and 90% is found, depending on altitude (Larsen et al., 2002).

For measurement M6, best agreement between PSC observation and theoretical data is found for water-rich LTA droplets (refractive index of 1.37) with diameters between 0.7 and 0.9 μm and a number density of 9–10 cm^{-3} . The amount of condensed HNO_3 (3.4–6.5 ppbv) is similar to the value retrieved for the LTA droplets of measurement M3. However, total reduction of gas-phase HNO_3 is less pronounced than in the latter case, since solid NAT particles do not contribute significantly. The reason for this is unclear, but one could speculate that the time span between particle nucleation and lidar observation was too short to permit the NAT particles to grow to optically relevant sizes (compare Figs. 5 and 7). In addition, cooling rates were lower in the afternoon than in the morning, so probably fewer NAT particles nucleated (Wirth et al., 1999; Fueglistaler et al., 2003). Finally, we note that retrieved LTA number densities of measurements M3 and M6 agree well with those reported previously (Voigt et al., 2000; Biele et al., 2001; Hu et al., 2002), while droplet diameters appear to be slightly larger (Voigt et al., 2000; Hu et al., 2002).

6. Summary

The clarification of the mechanisms that lead to the formation and dissipation of mountain wave-induced PSCs and the assessment of their microphysical properties will help to better understand stratospheric ozone chemistry. Our study demonstrates that ground-based lidar measurements can contribute to this endeavor if mesoscale meteorological modeling is employed to resolve the space-time ambiguity of the observations. In our approach, PSC microphysical properties are retrieved by comparison of the measured particle depolarization ratio and PSC-averaged lidar ratio to theoretical optical data obtained for different particle shapes. It is found that for relatively small

**Mountain wave PSC
dynamics and
microphysics**J. Reichardt et al.

particles retrieval results are stable because lidar ratio and depolarization ratio exhibit an opposite dependence on particle maximum dimension. However, this is not so with particles much larger than our observation wavelength of 355 nm and thus only a lower limit to the size of the PSC particles can be derived in this case. The micro-physical retrieval of the large PSC particles would have been improved considerably, if additionally depolarization and lidar ratios had been available at a longer wavelength, preferably at 1064 nm. Furthermore, our analysis suggests that model optical data of irregular particles and hexagonal particles rather than those of spheroids better represent, respectively, scattering by small and large PSC particles.

Acknowledgements. This work was funded by grants from NASA's Atmospheric Chemistry Modeling and Analysis Program, the European Commission, and the German Bundesministerium für Bildung, Wissenschaft und Technologie. JR would like to thank the other members of the former GKSS lidar team, R. Baumgart and A. Behrendt, and the Esrange staff for their technical support.

References

- Ansmann, A., Wandinger, U., Riebesell, M., Weitkamp, C., and Michaelis, W.: Independent measurement of extinction and backscatter profiles in cirrus clouds by using a combined Raman elastic-backscatter lidar, *Appl. Opt.*, 31, 7113–7131, 1992. [5836](#)
- Baumgarten, G.: Erste Messungen des Bonner Rayleigh/Mie/ Raman-Lidar auf Esrange, Schweden, zur Untersuchung von dynamisch induzierten polaren Stratosphärenwolken im Januar 1997, Diplomarbeit (Universität Bonn, Bonn, Germany), BONN-IB-97-26, 1997. [5835](#), [5868](#)
- Biele, J., Tsias, A., Luo, B. P., Carslaw, K. S., Neuber, R., Beyerle, G., and Peter, T.: Nonequilibrium coexistence of solid and liquid particles in Arctic stratospheric clouds, *J. Geophys. Res.*, 106, 22 991–23 007, 2001. [5837](#), [5857](#)
- Browell, E. V., Butler, C. F., Ismail, S., Robinette, P. A., Carter, A. F., Higdon, N. S., Toon, O. B., Schoeberl, M. R., and Tuck, A. F.: Airborne lidar observations in the wintertime Arctic stratosphere: polar stratospheric clouds, *Geophys. Res. Lett.*, 17, 385–388, 1990. [5835](#), [5837](#)

[Title Page](#)[Abstract](#)[Introduction](#)[Conclusions](#)[References](#)[Tables](#)[Figures](#)[◀](#)[▶](#)[◀](#)[▶](#)[Back](#)[Close](#)[Full Screen / Esc](#)[Print Version](#)[Interactive Discussion](#)

© EGU 2003

**Mountain wave PSC
dynamics and
microphysics**

J. Reichardt et al.

Title Page

Abstract

Introduction

Conclusions

References

Tables

Figures

◀

▶

◀

▶

Back

Close

Full Screen / Esc

Print Version

Interactive Discussion

© EGU 2003

Carslaw, K. S., Luo, B. P., Clegg, S. L., Peter, Th., Brimblecombe, P., and Crutzen, P. J.: Stratospheric aerosol growth and HNO₃ gas phase depletion from coupled HNO₃ and water uptake by liquid particles, *Geophys. Res. Lett.*, 21, 2479–2482, 1994. [5847](#), [5856](#)

Carslaw, K. S., Wirth, M., Tsias, A., Luo, B. P., Dörnbrack, A., Leutbecher, M., Volkert, H., Renger, W., Bacmeister, J. T., Reimers, E., and Peter, Th.: Increased stratospheric ozone depletion due to mountain-induced atmospheric waves, *Nature*, 391, 675–678, 1998a. [5847](#)

Carslaw, K. S., Wirth, M., Tsias, A., Luo, B. P., Dörnbrack, A., Leutbecher, M., Volkert, H., Renger, W., Bacmeister, J. T., and Peter, T.: Particle microphysics and chemistry in remotely observed mountain polar stratospheric clouds, *J. Geophys. Res.*, 103, 5785–5796, 1998b. [5833](#), [5845](#), [5846](#), [5851](#), [5853](#), [5854](#)

Deshler, T., Nardi, B., Adriani, A., Cairo, F., Hansen, G., Fierli, F., Hauchecorne, A., and Pulvirenti, L.: Determining the index of refraction of polar stratospheric clouds above Andoya (69° N) by combining size-resolved concentration and optical scattering measurements, *J. Geophys. Res.*, 105, 3943–3953, 2000. [5852](#)

Dörnbrack, A., Leutbecher, M., Kivi, R., and Kyrö, E.: Mountain wave induced record low stratospheric temperatures above northern Scandinavia, *Tellus*, 51A, 951–963, 1999. [5840](#)

Dörnbrack, A., Leutbecher, M., Reichardt, J., Behrendt, A., Müller, K.-P., and Baumgarten, G.: Relevance of mountain wave cooling for the formation of polar stratospheric clouds over Scandinavia: mesoscale dynamics and observations for January 1997, *J. Geophys. Res.*, 106, 1569–1581, 2001. [5834](#)

Dörnbrack, A., Birner, T., Fix, A., Flentje, H., Meister, A., Schmid, H., Browell, E. V., and Mahoney, M. J.: Evidence for inertia gravity waves forming polar stratospheric clouds over Scandinavia, *J. Geophys. Res.*, 107, D20, 8287, doi:10.1029/2001JD000452, 2002. [5833](#), [5839](#), [5840](#), [5844](#), [5849](#), [5857](#)

Dudhia, J.: A non-hydrostatic version of the Penn State–NCAR Mesoscale Model: validation tests and simulation of an Atlantic cyclone and cold front, *Mon. Weather Rev.*, 121, 1493–1513, 1993. [5839](#)

Dudhia, J., Gill, D., Guo, Y.-R., Manning, K., and Wang, W.: PSU/NCAR Mesoscale Modeling System Tutorial Class Notes and User Guide: MM5 Modeling System Version 3, 2001, also at <http://www.mmm.ucar.edu/mm5/>. [5839](#)

Echle, G., Oelhaf, H., and Wegner, A.: Measurement of atmospheric parameters with MIPAS, ESA Contract 9597/91/NL/SF Final Report, European Space Agency, 1992. [5870](#)

Fahey, D. W., Kelly, K. K., Ferry, G. V., Poole, L. R., Wilson, J. C., Murphy, D. M., Loewenstein,

**Mountain wave PSC
dynamics and
microphysics**

J. Reichardt et al.

Title Page

Abstract

Introduction

Conclusions

References

Tables

Figures

◀

▶

◀

▶

Back

Close

Full Screen / Esc

Print Version

Interactive Discussion

© EGU 2003

M., and Chan, K. R.: In situ measurements of total reactive nitrogen, total water, and aerosol in a polar stratospheric cloud in the Antarctic, *J. Geophys. Res.*, 94, 11299–11315, 1989. [5849](#)

5 Flentje, H., Dörnbrack, A., Fix, A., Meister, A., Schmid, H., Füglistaler, S., Luo, B., and Peter, T.: Denitrification inside the stratospheric vortex in the winter of 1999–2000 by sedimentation of large nitric acid trihydrate particles, *J. Geophys. Res.*, 107, D16, doi:10.1029/2001JD001015, 2002. [5851](#)

10 Fricke, K. H.: Lee wave modification of polar stratospheric clouds at the Scandinavian mountain ridge (LWPSC), *European Stratospheric Ozone Research 1996–1997*, edited by Amanatidis, G. T. and Harris, N., Vol. 59, *Air pollution research report*, EUR 16987, 71–74, 1997. [5833](#)

15 Fricke, K. H., Müller, K. P., Serwazi, M., Reichardt, J., Kirkwood, S., Steen, Å., Hoffmann, P., Mehrtens, H., Hauchecorne, A., Fierli, F., Hoppe, U. P., and Hansen, G.: Observations of dynamically induced polar stratospheric clouds in the lee of the Scandinavian mountain ridge, *Mesoscale processes in the stratosphere. Proceedings of the European workshop*, edited by Carslaw, K. S. and Amanatidis, G. T., Vol. 69, *Air pollution research report*, EUR 18912 EN, 81–86, 1999. [5838](#), [5843](#), [5850](#)

Fueglistaler, S., Buss, S., Luo, B. P., Wernli, H., Flentje, H., Hostetler, C. A., Poole, L. R., Carslaw, K. S., and Peter, Th.: Detailed modeling of mountain PSCs, *Atmos. Chem. Phys.*, 3, 697–712, 2003. [5833](#), [5847](#), [5851](#), [5854](#), [5857](#)

20 Gill, A. E: *Atmosphere-Ocean Dynamics*, Academic Press, New York, 1982. [5839](#)

Gobbi, G. P., Di Donfrancesco, G., and Adriani, A.: Physical properties of stratospheric clouds during the Antarctic winter of 1995, *J. Geophys. Res.*, 103, 10859–10873, 1998. [5837](#)

Hanson, D., and Mauersberger, K.: Laboratory studies of the nitric acid trihydrate: implications for the south polar stratosphere, *Geophys. Res. Lett.*, 15, 855–858, 1988. [5869](#)

25 Hess, M., Koелеmeijer, R. B. A., and Stammes, P.: Scattering matrices of imperfect hexagonal ice crystals, *J. Quant. Spectrosc. Radiat. Transfer*, 60, 301–308, 1998. [5872](#)

Hu, R.-M., Carslaw, K. S., Hostetler, C., Poole, L. R., Luo, B., Peter, T., Fueglistaler, S., McGee, T. J., and Burris, J. F.: Microphysical properties of wave polar stratospheric clouds retrieved from lidar measurements during SOLVE/THESEO 2000, *J. Geophys. Res.*, 107, D20, 8294, doi:10.1029/2001JD001125, 2002. [5833](#), [5851](#), [5852](#), [5854](#), [5857](#)

30 Kawa, S. R., Fahey, D. W., Kelly, K. K., Dye, J. E., Baumgardner, D., Gandrud, B. W., Loewenstein, M., Ferry, G. V., and Chan, K. R.: The Arctic polar stratospheric cloud aerosol: aircraft measurements of reactive nitrogen, total water, and particles, *J. Geophys. Res.*, 97, 7925–

7938, 1992. [5849](#)

- Larsen, N., Høyer Svendsen, S., Knudsen, B. M., Voigt, C., Weisser, C., Kohlmann, A., Schreiner, J., Mauersberger, K., Deshler, T., Kröger, C., Rosen, J. M., Kjome, N. T., Adriani, A., Cairo, F., Di Donfrancesco, G., Ovarlez, J., Ovarlez, H., Dörnbrack, A., and Birner, T.: Microphysical mesoscale simulations of polar stratospheric cloud formation constrained by in situ measurements of chemical and optical cloud properties, *J. Geophys. Res.*, 107, D20, 8301, doi:10.1029/2001JD000999, 2002. [5847](#), [5849](#), [5851](#), [5852](#), [5855](#), [5856](#), [5857](#), [5870](#)
- Liu, L., and Mishchenko, M. I.: Constraints of PSC particle microphysics derived from lidar observations, *J. Quant. Spectrosc. Radiat. Transfer*, 70, 817–831, 2001. [5851](#)
- Luo, B., Krieger, U. K., and Peter, T.: Densities and refractive indices of $\text{H}_2\text{SO}_4/\text{HNO}_3/\text{H}_2\text{O}$ solutions to stratospheric temperatures, *Geophys. Res. Lett.*, 23, 3707–3710, 1996. [5856](#)
- Marti, J., and Mauersberger, K.: Laboratory simulations of PSC particle formation, *Geophys. Res. Lett.*, 20, 359–362, 1993. [5849](#)
- Mishchenko, M. I.: Light scattering by randomly oriented axially symmetric particles, *J. Opt. Soc. Am. A*, 8, 871–882, 1991. [5852](#)
- Müller, K.-P., Baumgarten, G., Siebert, J., and Fricke, K. H.: The new lidar facility at Esrange, Kiruna, Proceedings, 13th ESA Symposium on European Rocket and Balloon Programmes and Related Research, Öland, Sweden, 26–29 May 1997, ESA SP-397, 129–134, 1997. [5833](#), [5835](#)
- Reichardt, J.: Error analysis of Raman differential absorption lidar ozone measurements in ice clouds, *Appl. Opt.*, 39, 6058–6071, 2000. [5838](#)
- Reichardt, J., Wandinger, U., Serwazi, M., and Weitkamp, C.: Combined Raman lidar for aerosol, ozone, and moisture measurements, *Opt. Eng.*, 35, 1457–1465, 1996. [5833](#), [5834](#)
- Reichardt, J., Hess, M., and Macke, A.: Lidar inelastic multiple-scattering parameters of cirrus particle ensembles determined with geometrical-optics crystal phase functions, *Appl. Opt.*, 39, 1895–1910, 2000a. [5838](#)
- Reichardt, J., Tsias, A., and Behrendt, A.: Optical properties of PSC Ia-enhanced at UV and visible wavelengths: model and observations, *Geophys. Res. Lett.*, 27, 201–204, 2000b. [5854](#)
- Reichardt, J., Reichardt, S., Behrendt, A., and McGee, T. J.: Correlations among the optical properties of cirrus-cloud particles: implications for spaceborne remote sensing, *Geophys. Res. Lett.*, 29, doi:10.1029/2002GL014836, 2002a. [5836](#), [5850](#)
- Reichardt, J., Reichardt, S., Hess, M., and McGee, T. J.: Correlations among the optical proper-

Mountain wave PSC dynamics and microphysics

J. Reichardt et al.

Title Page

Abstract

Introduction

Conclusions

References

Tables

Figures

◀

▶

◀

▶

Back

Close

Full Screen / Esc

Print Version

Interactive Discussion

**Mountain wave PSC
dynamics and
microphysics**

J. Reichardt et al.

[Title Page](#)[Abstract](#)[Introduction](#)[Conclusions](#)[References](#)[Tables](#)[Figures](#)[◀](#)[▶](#)[◀](#)[▶](#)[Back](#)[Close](#)[Full Screen / Esc](#)[Print Version](#)[Interactive Discussion](#)

© EGU 2003

ties of cirrus-cloud particles: microphysical interpretation, *J. Geophys. Res.*, 107, D21, 4562, doi:10.1029/2002JD002589, 2002b. [5836](#), [5872](#)

Reichardt, J., Reichardt, S., Yang, P., and McGee, T. J.: Retrieval of polar stratospheric cloud microphysical properties from lidar measurements: dependence on particle shape assumptions, *J. Geophys. Res.*, 107, D20, 8282, doi:10.1029/2001JD001021, 2002c. [5834](#), [5835](#), [5836](#), [5851](#), [5852](#)

Reichardt, J., Baumgart, R., and McGee, T. J.: Three-signal method for accurate measurements of depolarization ratio with lidar, *Appl. Opt.*, 42, 4909–4913, 2003. [5836](#)

Schotland, R. M., Sassen, K., and Stone, R.: Observations by lidar of linear depolarization ratios for hydrometeors, *J. Appl. Meteorol.*, 10, 1011–1017, 1971. [5836](#)

Schreiner, J., Voigt, C., Weisser, C., Kohlmann, A., Mauersberger, K., Deshler, T., Kröger, C., Rosen, J., Kjome, N., Larsen, N., Adriani, A., Cairo, F., Di Donfrancesco, G., Ovarlez, J., Ovarlez, H., and Dörnbrack, A.: Chemical, microphysical, and optical properties of polar stratospheric clouds, *J. Geophys. Res.*, 107, 8313, doi:10.1029/2001JD000825, 2002. [printed in 108, D5, 2003] [5849](#), [5857](#)

Stein, B., Wedekind, C., Wille, H., Immler, F., Müller, M., Wöste, L., del Guasta, M., Morandi, M., Stefanutti, L., Antonelli, A., Agostini, P., Rizi, V., Readelli, G., Mitev, V., Matthey, R., Kivi, R., and Kyrö, E.: Optical classification, existence temperatures, and coexistence of different polar stratospheric cloud types, *J. Geophys. Res.*, 104, 23983–23993, 1999. [5837](#)

Tabazadeh, A., Toon, O. B., and Jensen, E. J.: Formation and implications of ice particle nucleation in the stratosphere, *Geophys. Res. Lett.*, 24, 2007–2010, 1997. [5846](#)

Tsias, A., Wirth, M., Carslaw, K. S., Biele, J., Mehrtens, H., Reichardt, J., Wedekind, C., Weiß, V., Renger, W., Neuber, R., von Zahn, U., Stein, B., Santacesaria, V., Stefanutti, L., Fierli, F., Bacmeister, J., and Peter, T.: Aircraft lidar observations of an enhanced type Ia polar stratospheric cloud during APE–POLECAT, *J. Geophys. Res.*, 104, 23 961–23 969, 1999. [5833](#), [5851](#), [5852](#), [5853](#), [5854](#)

Toon, O. B., Tabazadeh, A., Browell, E. V., and Jordan, J.: Analysis of lidar observations of Arctic polar stratospheric clouds during January 1989, *J. Geophys. Res.*, 105, 20 589–20 615, 2000. [5837](#), [5852](#), [5853](#)

van de Hulst, H. C.: *Light Scattering by Small Particles*, Dover, New York, 1981. [5852](#)

Voigt, C., Schreiner, J., Kohlmann, A., Zink, P., Mauersberger, K., Larsen, N., Deshler, T., Kröger, C., Rosen, J., Adriani, A., Cairo, F., Di Donfrancesco, G., Viterbini, M., Ovarlez, J., Ovarlez, H., David, C., and Dörnbrack, A.: Nitric acid trihydrate (NAT) in polar stratospheric

**Mountain wave PSC
dynamics and
microphysics**J. Reichardt et al.

[Title Page](#)[Abstract](#)[Introduction](#)[Conclusions](#)[References](#)[Tables](#)[Figures](#)[◀](#)[▶](#)[◀](#)[▶](#)[Back](#)[Close](#)[Full Screen / Esc](#)[Print Version](#)[Interactive Discussion](#)

© EGU 2003

clouds, *Science*, 290, 1756–1758, 2000. [5849](#), [5851](#), [5856](#), [5857](#)

Voigt, C., Larsen, N., Deshler, T., Kröger, C., Schreiner, J., Mauersberger, K., Luo, B., Adriani, A., Cairo, F., Di Donfrancesco, G., Ovarlez, J., Ovarlez, H., Dörnbrack, A., Knudsen, B., and Rosen, J.: In situ mountain-wave polar stratospheric cloud measurements: implications for nitric acid trihydrate formation, *J. Geophys. Res.*, 108, D5, 8331, doi:10.1029/2001JD001185, 2003. [5854](#)

Wandinger, U.: Multiple-scattering influence on extinction- and backscatter-coefficient measurements with Raman and high-spectral-resolution lidars, *Appl. Opt.*, 37, 417–427, 1998. [5838](#)

Warren, S. G.: Optical constants of ice from the ultraviolet to the microwave, *Appl. Opt.*, 23, 1206–1225, 1984. [5852](#)

Waterman, P. C.: Symmetry, unitarity, and geometry in electromagnetic scattering, *Phys. Rev. D*, 3, 825–839, 1970. [5852](#)

Wirth, M., Tsias, A., Dörnbrack, A., Weiß, V., Carslaw, K. S., Leutbecher, M., Renger, W., Volkert, H., and Peter, T.: Model-guided Lagrangian observation and simulation of mountain polar stratospheric clouds, *J. Geophys. Res.*, 104, 23 971–23 981, 1999. [5833](#), [5844](#), [5845](#), [5851](#), [5852](#), [5853](#), [5854](#), [5856](#), [5857](#)

Yang, P., Liou, K. N., Mishchenko, M. I., and Gao, B.-C.: Efficient finite-difference time-domain scheme for light scattering by dielectric particles: application to aerosols, *Appl. Opt.*, 39, 3727–3737, 2000. [5852](#)

Zängl, G.: Stratified flow over a mountain with a gap: linear theory and numerical simulations, *Q. J. R. Meteorol. Soc.*, 128, 927–949, 2002. [5839](#)

Mountain wave PSC dynamics and microphysics

J. Reichardt et al.

Table 1. PSC optical (355 nm) and retrieved microphysical properties. COMP, RI, AR, and MD denote composition, refractive index, aspect ratio, and maximum dimension, respectively.

Measurement	δ_{par}	S_{par} SF	$R - 1$	COMP	RI	Shape	AR	MD μm	n cm^{-3}	HNO_3 condensed
M1–M3	0.25–0.35	70 ± 14	0.3	NAT	1.53	irregular	0.75–1.25	0.7–0.9	8–12	4.5–7.6
M3	0	70 ± 14	0.6	LTA	1.39	spherical	1	0.7–0.9	7–11	3.7–4.8
M4	0.52–0.64	20 ± 4	15–20	ice	1.32	irr., hex.		> 4.3	≤ 5	0
M5	0.55–0.65	35 ± 7	10	ice	1.32	irregular	0.75–1	> 1.9	< 27	0
							1 ^a	3–3.5	8–11 ^a	
M6	0	113 ± 22	0.7	LTA	1.37	spherical	1	0.7–0.9	9–10	3.4–6.5

^a = assumed value.

Title Page

Abstract

Introduction

Conclusions

References

Tables

Figures

◀

▶

◀

▶

Back

Close

Full Screen / Esc

Print Version

Interactive Discussion

© EGU 2003

Mountain wave PSC dynamics and microphysics

J. Reichardt et al.

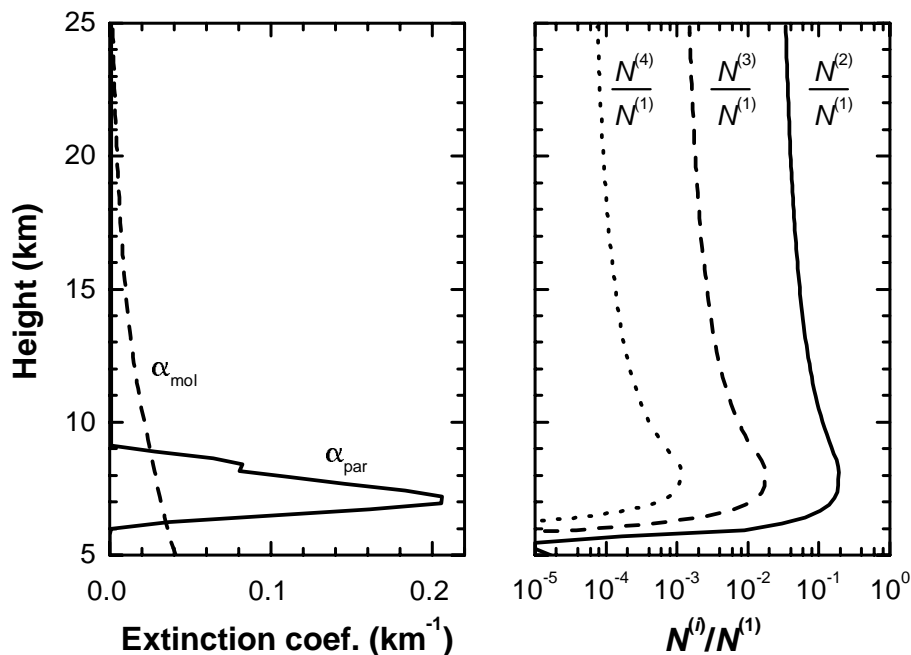


Fig. 1. Cirrus extinction profile (α_{par} ; observed over Esrange on 16 January 1997 between 22:06 and 22:46 UT), and molecular extinction (α_{mol} ; 16 January 1997 radiosonde data) (left), and modeled ratios of multiply to singly scattered light (right). For the multiple-scattering calculations the cirrus cloud is assumed to consist of columnar crystals with maximum dimensions between 20 and 700 μm ; the laser wavelength is 355 nm; and the lidar field of view is 0.6 mrad.

Title Page

Abstract

Introduction

Conclusions

References

Tables

Figures

◀

▶

◀

▶

Back

Close

Full Screen / Esc

Print Version

Interactive Discussion

© EGU 2003

Mountain wave PSC dynamics and microphysics

J. Reichardt et al.

Title Page

Abstract

Introduction

Conclusions

References

Tables

Figures

◀

▶

◀

▶

Back

Close

Full Screen / Esc

Print Version

Interactive Discussion

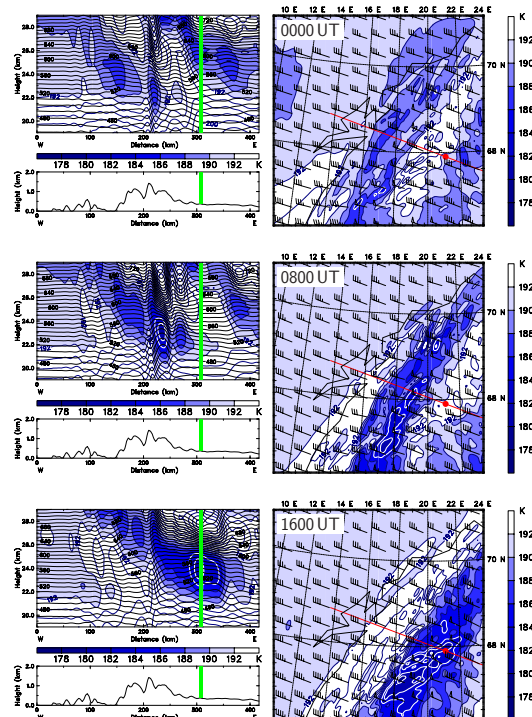


Fig. 2. Temperature $T \leq 192$ K (color shaded; K) at the 550-K isentropic surface (right) and along the vertical section as indicated by the red line (left) on 16 January 1997. Additional fields on the right: horizontal wind vectors (barbs; long: 10 ms^{-1} , short: 5 ms^{-1}) and $T \leq 184$ K (white lines; $\Delta T = 2$ K). On the left: potential temperature Θ (solid black lines; $\Delta\Theta = 10$ K, 550-K isentropes bold) and temperature (solid blue lines; $\Delta T = 2$ K); here again, white lines mark regions with $T \leq 184$ K. The position of the lidar site at Esrange is marked (red dot in the horizontal and thick green line in the vertical section). The profile of the model orography is plotted below each vertical section. Numerical results are from the innermost domain of the mesoscale model ($\Delta x = 3$ km).

Mountain wave PSC dynamics and microphysics

J. Reichardt et al.

Title Page

Abstract

Introduction

Conclusions

References

Tables

Figures

◀

▶

◀

▶

Back

Close

Full Screen / Esc

Print Version

Interactive Discussion

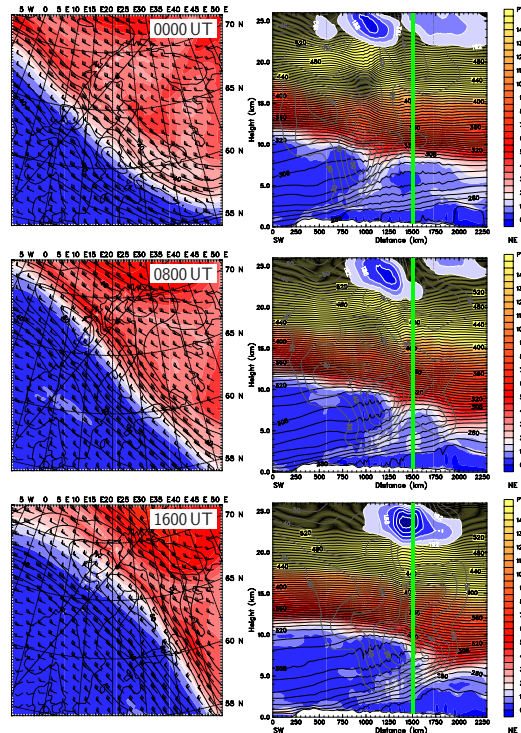


Fig. 3. Potential vorticity (color shaded; PVU, where $1 \text{ PVU} = 10^{-6} \text{ K m}^2 \text{ kg}^{-1} \text{ s}^{-1}$) on the 308-K isentropic surface (left) and along the vertical section as indicated by the black line (right) on 16 January 1997. Additional fields on the left: horizontal wind vectors (barbs; long: 10 ms^{-1} , short: 5 ms^{-1}) and horizontal wind speed $> 40 \text{ ms}^{-1}$ (black solid lines; 5 ms^{-1} increment). On the right: potential temperature Θ (thin black solid lines; $\Delta\Theta = 4 \text{ K}$, 308-K isentrope bold), horizontal wind speed $> 40 \text{ ms}^{-1}$ (thick solid lines; 5 ms^{-1} increment), and stratospheric temperature $T \leq 192 \text{ K}$ (color shaded as in Fig. 2 for heights $> 20 \text{ km}$; K). The position of the lidar site at Erange is marked (black dot in the horizontal and thick green line in the vertical section). Numerical results are from the coarse grid domain of the mesoscale model ($\Delta x = 27 \text{ km}$).

Mountain wave PSC dynamics and microphysics

J. Reichardt et al.

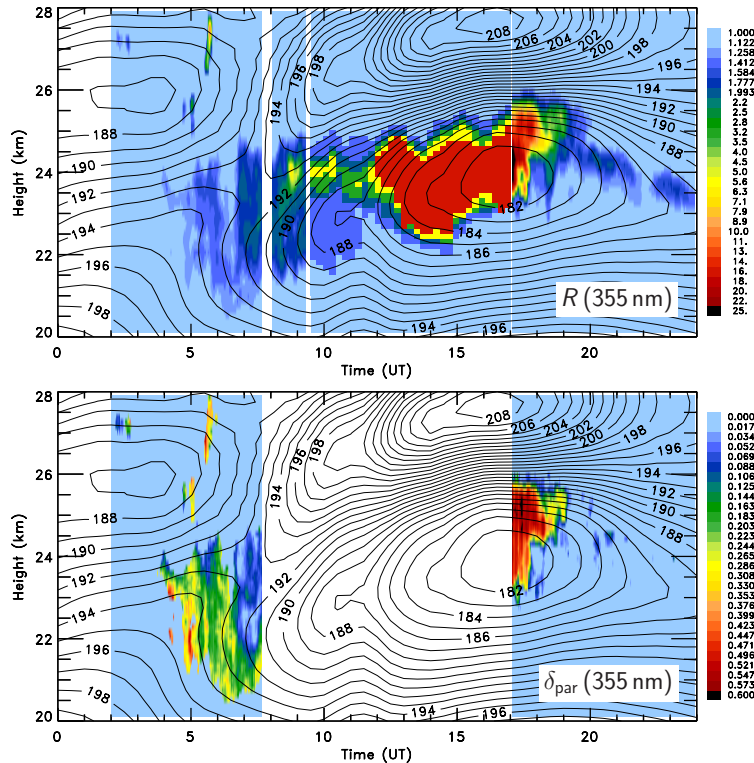


Fig. 4. Temporal evolution of 355-nm backscatter ratio R and of 355-nm particle depolarization ratio δ_{par} on 16 January 1997 over Esrange. Superimposed is the temperature (solid lines; K) from the innermost domain of the mesoscale numerical simulation ($\Delta x = 3$ km). Backscatter-ratio data between 09:30 and 17:00 UT were taken from Baumgarten (1997). The original measurements at a wavelength of 532 nm (parallel polarization only) were converted to 355-nm R values assuming wavelength-independent particle scattering. In view of the coarse gradation of the 532-nm data available, no effort was made to account for their polarization sensitivity.

Title Page

Abstract

Introduction

Conclusions

References

Tables

Figures

◀

▶

◀

▶

Back

Close

Full Screen / Esc

Print Version

Interactive Discussion

© EGU 2003

Mountain wave PSC dynamics and microphysics

J. Reichardt et al.

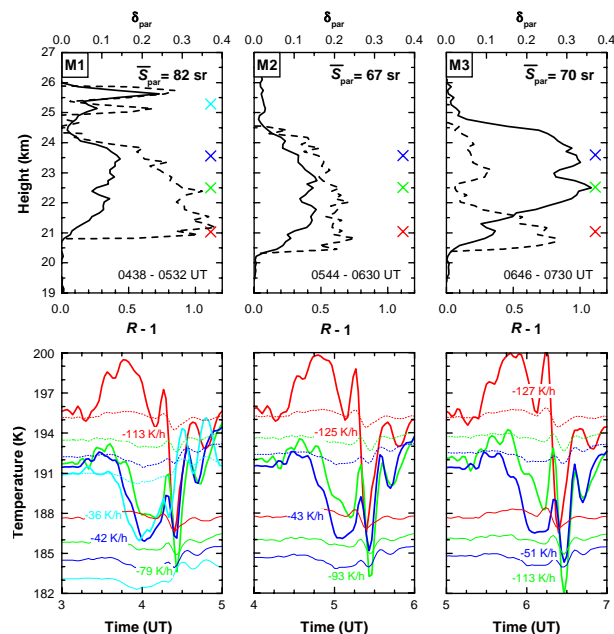


Fig. 5. Backscatter ratio R (solid curves) and particle depolarization ratio δ_{par} (dashed curves) of the mountain wave PSC as observed with the GKSS Raman lidar in the morning of 16 January 1997 (top panels). Mean lidar ratio \bar{S}_{par} is indicated. Lidar data were integrated over measurement intervals with similar PSC optical and geometrical properties (M1–M3). The vertical resolution is 120 m, the measurement wavelength is 355 nm. Air parcel temperature histories derived from mesoscale numerical simulations (bottom panels). Starting at 05:00, 06:00, and 07:00 UT (about the center times of M1–M3) and at various heights (colored symbols, top panels), the trajectories are calculated backward in time. Ambient temperatures (solid curves), frost point temperatures (thin solid curves) and NAT equilibrium temperatures (thin dashed curves; calculated according to [Hanson and Mauersberger \(1988\)](#)) are shown. A water vapor concentration of 5 ppmv and a HNO_3 profile (Fig. 6) are assumed. Maximum cooling rates are indicated. Temperatures and cooling rate are shown in the color of the corresponding start height.

Title Page

Abstract

Introduction

Conclusions

References

Tables

Figures

◀

▶

◀

▶

Back

Close

Full Screen / Esc

Print Version

Interactive Discussion

Mountain wave PSC dynamics and microphysics

J. Reichardt et al.

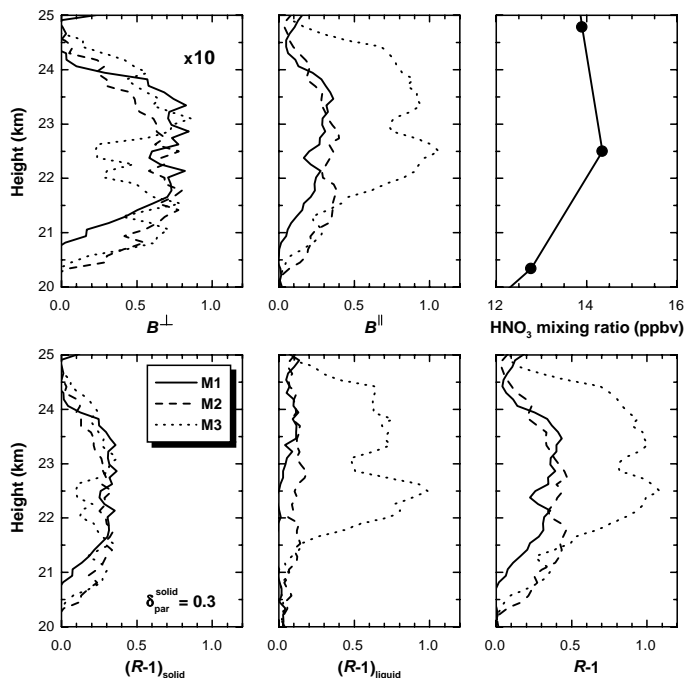


Fig. 6. Coexistence of solid and liquid PSC particles observed in the morning of 16 January 1997. Ratio of perpendicular-polarized particle backscatter coefficient to molecular backscatter coefficient (B^\perp), ratio of parallel-polarized particle backscatter coefficient to molecular backscatter coefficient (B^\parallel), and scattering contributions of solid [$(R - 1)_{\text{solid}}$] and liquid [$(R - 1)_{\text{liquid}}$] particles to the PSC backscatter ratio $(R - 1)$ for measurement intervals M1–M3. $(R - 1)_{\text{solid}}$ and $(R - 1)_{\text{liquid}}$ are retrieved under the assumption that solid particles at all PSC heights have depolarization ratios similar to those measured below 22.5 km during time period M1 (~ 0.3). The HNO_3 profile used for the calculation of T_{NAT} is also shown (top, right); it was generated by scaling the polar HNO_3 profile of [Echle et al. \(1992\)](#) so that maximum HNO_3 values within the PSC layer agree with those observed in situ in a similar mountain-wave PSC case ([Larsen et al., 2002](#)).

Title Page

Abstract

Introduction

Conclusions

References

Tables

Figures

◀

▶

◀

▶

Back

Close

Full Screen / Esc

Print Version

Interactive Discussion

© EGU 2003

Mountain wave PSC
dynamics and
microphysics

J. Reichardt et al.

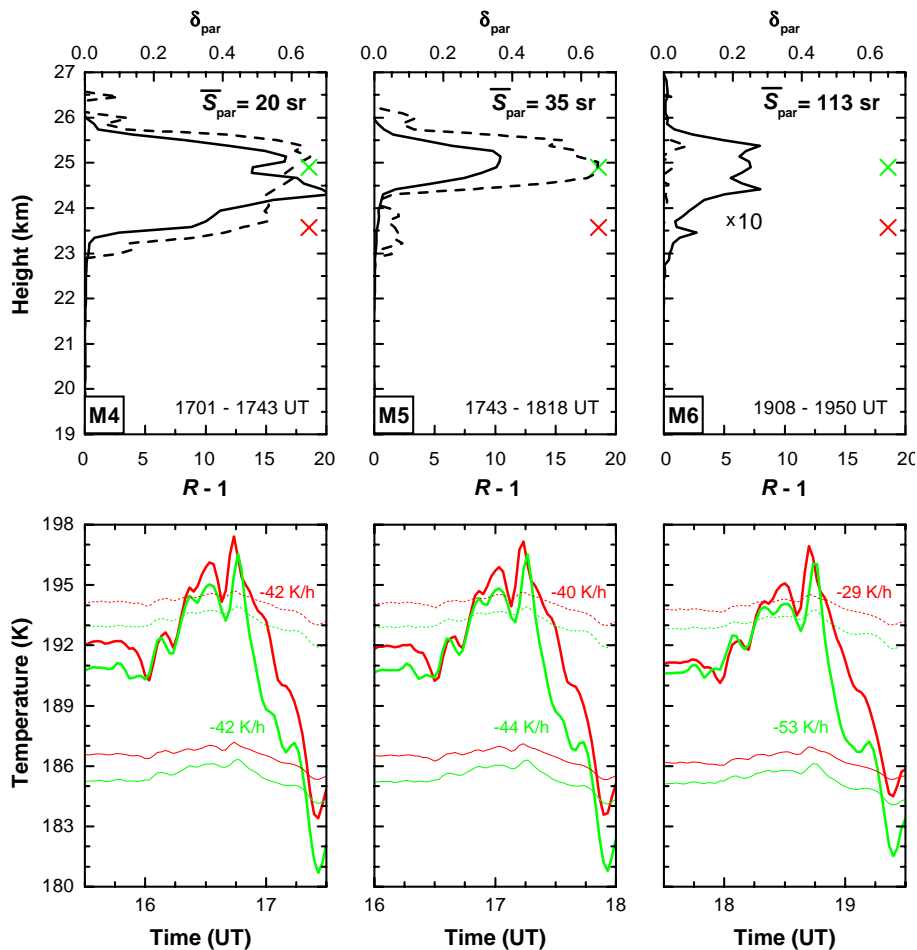


Fig. 7. Same as in Fig. 5, but for the afternoon of 16 January 1997 (measurements M4–M6). Backscatter ratio of measurement M6 was multiplied by a factor of ten.

[Title Page](#)[Abstract](#)[Introduction](#)[Conclusions](#)[References](#)[Tables](#)[Figures](#)[◀](#)[▶](#)[◀](#)[▶](#)[Back](#)[Close](#)[Full Screen / Esc](#)[Print Version](#)[Interactive Discussion](#)

© EGU 2003

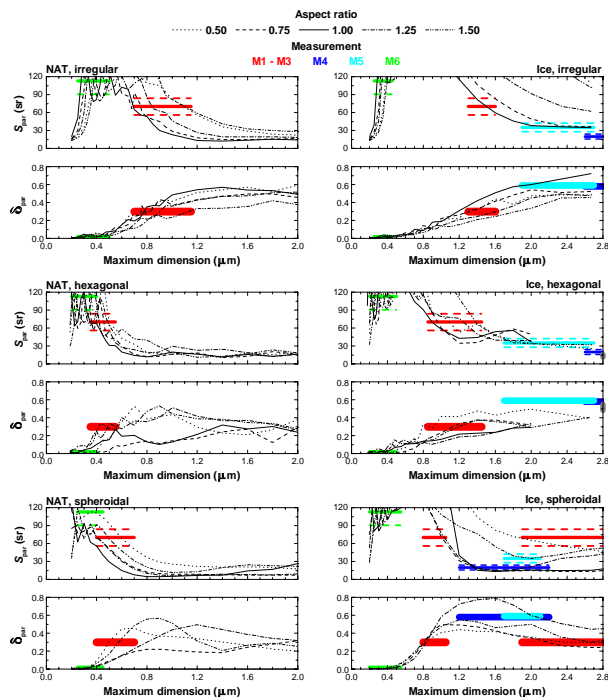


Fig. 8. Retrieval of microphysical properties of solid PSC particles from measurements M1–M6. Measured data are visualized with solid horizontal lines, line lengths and positions indicate particle size ranges that show best agreement between observations and theoretical data. Horizontal line thickness of measured δ_{par} indicates variability of the PSC profile, dashed horizontal lines show estimated systematic errors of S_{par} . Note that displayed ranges of maximum dimension are different for NAT and ice particles. Theoretical optical data of irregular and hexagonal particles, spheroids (aspect ratios $\neq 1$), and spheres were obtained with, respectively, finite-difference time-domain, T-matrix, and Mie computations. Results of geometrical-optics calculations for hexagonal ice columns are also shown (gray marks, center, right; aspect ratios between 1 and 2.5, slightly distorted shape, see Hess et al., 1998; Reichardt et al., 2002b). The wavelength is 355 nm.

Title Page

Abstract

Introduction

Conclusions

References

Tables

Figures

◀

▶

◀

▶

Back

Close

Full Screen / Esc

Print Version

Interactive Discussion

Mountain wave PSC dynamics and microphysics

J. Reichardt et al.

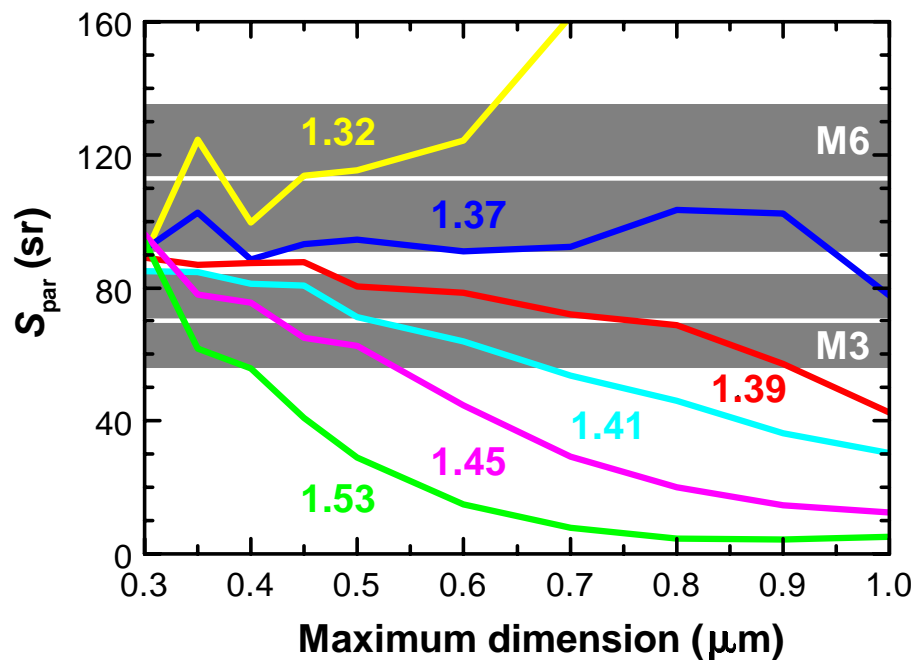


Fig. 9. Retrieval of microphysical properties of liquid PSC particles from measurements M3 and M6. Measured S_{par} data are indicated with white horizontal lines, shaded areas visualize estimated systematic errors. Mie theory was applied to calculate the optical properties of LTA droplets, assuming different chemical compositions (refractive indices are indicated). Computational results obtained for pure water ice and NAT are shown for comparison (refractive index of 1.32 and 1.53, respectively). The wavelength is 355 nm.

Title Page

Abstract

Introduction

Conclusions

References

Tables

Figures

◀

▶

◀

▶

Back

Close

Full Screen / Esc

Print Version

Interactive Discussion

© EGU 2003